J. Fluid Mech. (1989), *vol.* 207, *pp.* 267–294
Printed in Great Britain

Selection of convective planform orientation by boundary anisotropy

By ARNE J. PEARLSTEIN AND ALPARSLAN OZTEKIN
Department of Aerospace and Mechanical Engineering, University of Arizona, Tucson, AZ 85721, USA

(Received 5 April 1988 and in revised form 17 March 1989)

Thermal instability of a fluid layer confined between isotropic horizontal solid walls leads to convection cells having no preferred horizontal direction. For thermally anisotropic walls, we find that certain planform orientations are preferred, in that convection sets in at a smaller Rayleigh number (Ra) for some orientations than for others, thus providing a means by which a regular planform may be established in a large-aspect-ratio layer. We consider horizontal layers of two Boussinesq, Newtonian fluids separated by a rigid, thermally anisotropic plate of constant thickness. The upper and lower fluid layers are bounded above and below, respectively, by rigid, thermally anisotropic plates of arbitrary thickness. When the bounding surfaces are thermally anisotropic, the horizontal wavevector ($\boldsymbol{a}$) of the resulting convective flow has two distinct components. Thus, instead of a neutral curve in the (Ra, a)-plane, there is a neutral surface, and Ra depends on both components of $\boldsymbol{a}$, or alternatively, on $|\boldsymbol{a}|$ and the planform orientation angle $\Phi_r \in [0, 2\pi]$. In the isotropic case, the neutral surface is axisymmetric (i.e. invariant with respect to Φ_r), consistent with the known dependence on $|\boldsymbol{a}|$ only.

For anisotropic walls, axisymmetry is replaced by π-periodicity in the Φ_r direction, corresponding to invariance with respect to a 180° rotation, and the neutral surface has an even number of local minima. We study the dependence of Φ_r on the middle plate orientation (Φ_p). Several different Φ_r–Φ_p topologies are found. When the number of local minima exceeds two, discontinuous Φ_r–Φ_p plots may occur. The dependence of Φ_r on the thicknesses and conductivities of the plates and fluids and on the orientation of the plates is discussed, with special reference to the transitions between different $\Phi_r - \Phi_p$ topologies.

1. Introduction

The onset of convection in a motionless horizontal fluid layer heated from below and the transition to flows of increasing spatial and temporal complexity which occurs as the temperature difference (ΔT) increases have been the subject of considerable experimental and theoretical work. A problem of continuing interest is that of horizontal planform selection.

In containers of small to moderate aspect ratio (ratio of horizontal to vertical dimensions), the planform (shape and orientation of the convection cells) is determined by the nature of the fluid and the sidewall boundaries for ΔT well in excess of the value at which the motionless conduction state loses its stability.

For high-aspect-ratio containers, sidewall effects are confined to the periphery of the layer. Thus, although the planform *shape* may be determined by the fluid (e.g. hexagons are preferred over two-dimensional rolls if the viscosity depends sufficiently

strongly on temperature, as shown by Busse (1967*a*, *b*)), the remoteness of the sidewalls and the horizontal isotropy of the layer in its interior provide little basis for the selection of planform *orientation*. Thus, in high-aspect-ratio layers a regular planform may not exist, even for ΔT very close to the onset of convection (Ahlers & Behringer 1978; Proctor & Jones 1988).

The first experimental work concerned with convective planform selection in a high-aspect-ratio fluid layer was that of Chen & Whitehead (1968), in which convection cells having a preferred orientation (wavevector magnitude and direction) were generated by establishing well-defined initial conditions. Further theoretical and experimental investigation by Busse & Whitehead (1971) demonstrated that two-dimensional convection cells change to a three-dimensional pattern as the Rayleigh number is raised to about ten times its critical value. This suggests that planform orientation in a high-aspect-ratio layer can be selected by removing the horizontal isotropy in the interior.

In this work, we investigate the case in which convection cells in a horizontally infinite fluid layer have a preferred direction due to the thermal anisotropy of the boundaries. The existence of a preferred horizontal direction means that the planform must be described by a wavevector $\boldsymbol{a}$ with components a_x and a_y, and that the magnitude $a = |\boldsymbol{a}|$ is insufficient to describe the motion. Previous convective stability calculations in which two components of the wavevector are required include the investigation by Chandrasekhar (1954) of a layer subject to a horizontal magnetic field.

To this end, we have considered the onset of convection in a pair of fluid layers, separated by a rigid plate having finite thickness and thermal conductivity, previously investigated by Gershuni & Zhukhovitskii (1976), Catton & Lienhard (1984), Lienhard (1987), Hieber (1987), and Proctor & Jones (1988).

We have generalized the two-fluid analysis of Catton & Lienhard (1984) and Lienhard (1987) by considering top and bottom walls of non-zero thickness and finite conductivity, by taking all three bounding plates to be thermally anisotropic, and by allowing the two fluid layers to have different thermophysical properties. The focus of our work will be to study the effect of plate orientation on planform orientation and the use of boundary anisotropy to control planform orientation in thermal convection.

In addition to their fundamental interest, the results may be relevant to applications in which spatially regular convection in a large-aspect-ratio fluid layer is preferred to randomly oriented convection. One such application is the solidification of aligned magnetic composites and other anisotropic materials from the melt. If the fluid is electrically conducting, establishment of a preferred horizontal direction can be achieved by application of a horizontal magnetic field (Larson 1987). The use of boundary thermal anisotropy may allow horizontal alignment to be effected in a weakly conducting or non-conducting fluid.

The paper is organized as follows: In §2, we present the governing equations. The motionless conduction solution is given in §3. In §4, the linear stability analysis is presented. The reduction to two matrix eigenvalue problems and the solution technique are described in §5. The results are presented in §6 and discussed in §7.

2. The governing equations

The geometry of the problem is shown in figure 1. Two horizontal incompressible, viscous fluid layers of thicknesses L_2 and L_4 are bounded by three anisotropic

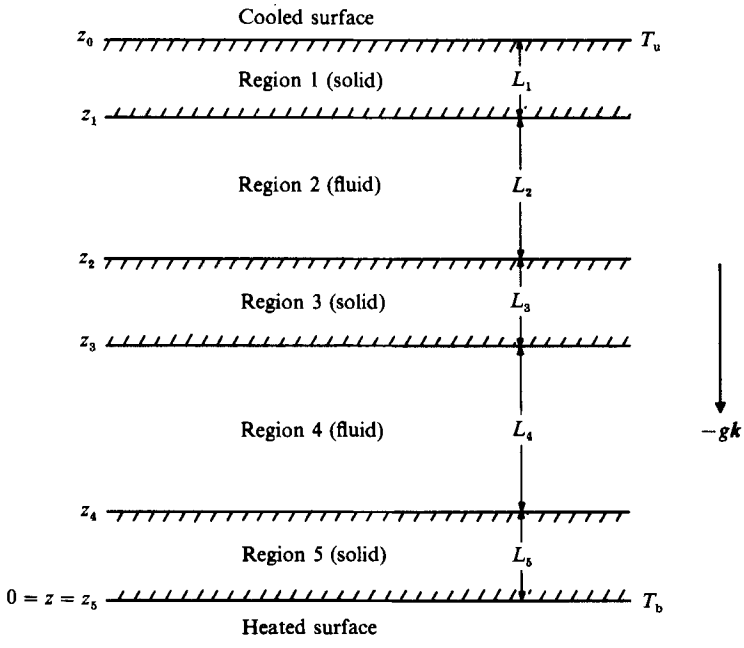

FIGURE 1. Physical configuration of the problem.

horizontal solid walls of thicknesses L_1, L_3 and L_5 with thermal conductivity tensors $\boldsymbol{k}_1$, $\boldsymbol{k}_3$ and $\boldsymbol{k}_5$. The upper and lower surfaces have temperatures T_u and T_b, respectively, with $T_b > T_u$. The fluid layers may have different thermal conductivities $\boldsymbol{k}_j$, kinematic viscosities ν_j, densities ρ_j, and heat capacities c_{pj}. We assume that the fluid layers satisfy the Boussinesq approximation, in which we neglect thermal variations of the fluid properties, except density in the buoyancy force. The viscous dissipation term in the fluid-phase energy equations is zero for the motionless basic state and is absent from the linear stability analysis which we use to study the onset of convection. Hence, it may be omitted.

The resulting equations governing the fluid motion are the standard Oberbeck–Boussinesq equations

$$\left.\begin{aligned} \boldsymbol{\nabla}\cdot\boldsymbol{v} &= 0, \qquad (2.1)\\ \frac{\mathrm{D}\boldsymbol{v}}{\mathrm{D}t} &= -\frac{1}{\rho_{j0}}\boldsymbol{\nabla}p - \frac{\rho_j}{\rho_{j0}}g\boldsymbol{k} + \nu_j\nabla^2\boldsymbol{v}, \qquad (2.2)\end{aligned}\right\} \quad j = 2, 4,$$

along with the energy equations

$$\frac{\mathrm{D}T}{\mathrm{D}t} = \kappa_j\nabla^2 T, \quad j = 2, 4, \qquad (2.3)$$

and equations of state $\rho_j = \rho_{j0}[1-\beta_j(T-T_0)]$ in the fluid layers, where $(\,)_0$ denotes the reference state. In the solid layers, we have

$$(\rho c_p)_j\frac{\partial T}{\partial t} = \boldsymbol{\nabla}\cdot(\boldsymbol{k}_j\boldsymbol{\nabla}T), \quad j = 1, 3, 5. \qquad (2.4)$$

We impose the no-slip condition

$$\boldsymbol{v}(x, y, z, t) = \boldsymbol{0} \qquad (2.5)$$

at the solid walls. The thermal boundary conditions are

$$T(x,y,z,t) = T_u \quad \text{at} \quad z = z_0,$$

$$T(x,y,z,t) = T_b \quad \text{at} \quad z = z_5.$$

We also require that the temperature and normal component of the heat flux be continuous at each interface:

$$T(x,y,z,t) \quad \text{continuous at } z_1, z_2, z_3, z_4, \tag{2.6}$$

$$\boldsymbol{n}\cdot\boldsymbol{q}(x,y,z,t) \quad \text{continuous at } z_1, z_2, z_3, z_4. \tag{2.7}$$

3. The basic state

Before proceeding to the analysis of the convective stability problem, we consider the conductive base state, in which $\boldsymbol{v} = \boldsymbol{0}$. We then have steady one-dimensional conduction in the solid and motionless fluid layers, so that $T_j = s_{j,1}z + s_{j,2}$, where $s_{j,1}$ and $s_{j,2}$ are constant in each layer. From elementary considerations (Carslaw & Jaeger 1959), we obtain temperature profiles for regions 1–5:

Region 1

$$\bar{T} = T_b - (T_b - T_u)\frac{1+h_2\gamma_2+h_3\gamma_3+h_5\gamma_5+(z-z_1)/(L_4\gamma_1)}{1+h_1\gamma_1+h_2\gamma_2+h_3\gamma_3+h_5\gamma_5}, \quad z_1 \leqslant z \leqslant z_0,$$

Region 2

$$\bar{T} = T_b - (T_b - T_u)\frac{1+h_3\gamma_3+h_5\gamma_5+(z-z_2)/(L_4\gamma_2)}{1+h_1\gamma_1+h_2\gamma_2+h_3\gamma_3+h_5\gamma_5}, \quad z_2 \leqslant z \leqslant z_1,$$

Region 3

$$\bar{T} = T_b - (T_b - T_u)\frac{1+h_5\gamma_5+(z-z_3)/(L_4\gamma_3)}{1+h_1\gamma_1+h_2\gamma_2+h_3\gamma_3+h_5\gamma_5}, \quad z_3 \leqslant z \leqslant z_2,$$

Region 4

$$\bar{T} = T_b - (T_b - T_u)\frac{h_5\gamma_5+(z-z_4)/L_4}{1+h_1\gamma_1+h_2\gamma_2+h_3\gamma_3+h_5\gamma_4}, \quad z_4 \leqslant z \leqslant z_3,$$

Region 5

$$\bar{T} = T_b - (T_b - T_u)\frac{(z-z_5)/(L_4\gamma_5)}{1+h_1\gamma_1+h_2\gamma_2+h_3\gamma_3+h_5\gamma_5}, \quad z_5 \leqslant z \leqslant z_4,$$

where we have defined $\gamma_2 = k_4/k_2$, $h_j = L_j/L_4$ for $j = 1, 2, 3, 5$, and $\gamma_j = k_4/k_{zz,j}$ for $j = 1, 3, 5$.

4. Linear stability analysis

To determine the conditions under which disturbances grow, we superimpose perturbations T', p', and $\boldsymbol{v}'$ on the motionless base state, substitute into (2.1)–(2.4), cancel terms associated with the motionless solution, and linearize (as is appropriate for infinitesimal disturbances) to obtain the disturbance equations

$$\left.\begin{aligned} \nabla\cdot\boldsymbol{v}' &= 0, \\ \frac{\partial\boldsymbol{v}'}{\partial t} &= -\frac{1}{\rho_{j0}}\nabla p' + g\beta_j T'\boldsymbol{k} + \nu_j\nabla^2\boldsymbol{v}', \\ \frac{\partial T'}{\partial t} + \boldsymbol{v}'\cdot\nabla T_s &= \kappa_j\nabla^2 T', \end{aligned}\right\} \quad j = 2, 4$$

for the fluid layers. For the anisotropic solid plates, we have simply

$$(\rho c_p)_j \frac{\partial T'}{\partial t} = \nabla \cdot (\boldsymbol{k}_j \nabla T'), \quad j = 1, 3, 5.$$

The boundary conditions for the disturbances are the same as (2.5)–(2.7), with $T'(x, y, z_0, t) = 0$ and $T'(x, y, z_5, t) = 0$.

To eliminate the pressure, we twice take the curl of each momentum equation and then take the vertical component. We obtain non-dimensional equations in the jth fluid layer by using the scaling: velocity ν_j/L_j; temperature $\Delta T_j = \bar{T}(z_j) - \bar{T}(z_{j-1})$; time L_j^2/κ_j; length L_j. The scaled coordinates are defined by $z_i' = (z - z_i)/L_i$ for $z_i \leqslant z \leqslant z_{i-1}$.

The governing non-dimensional equations for the fluid layers become

$$\left.\begin{aligned} \frac{\partial}{\partial \tau_j} \nabla_j'^2 W_j' &= Ra_j \nabla_{j\perp}'^2 \Theta_j' + Pr_j \nabla_j'^4 W_j', \qquad (4.1) \\ \frac{\partial \Theta_j'}{\partial \tau_j} &= \nabla_j'^2 \Theta_j' + Pr_j W_j', \qquad (4.2) \end{aligned}\right\} \quad j = 2, 4,$$

where $\nabla_{j\perp}'^2 = \partial^2/\partial x_j'^2 + \partial^2/\partial y_j'^2$ is the horizontal Laplacian, $Ra_j = \beta_j \Delta T_j L_j^3 g/(\nu_j \kappa_j)$, $Pr_j = \nu_j/\kappa_j$, for $j = 2, 4$, and all quantities are non-dimensional. The governing equations for the solid walls are

$$\frac{\partial \Theta_j}{\partial \tau_j} = \nabla_j' \cdot \left[\frac{\boldsymbol{k}_j}{k_{zz,j}} \nabla_j' \Theta_j\right], \quad j = 1, 3, 5. \tag{4.3}$$

The disturbance satisfies the boundary conditions

$$W_j'(x_j', y_j', 0, \tau_j) = W_j'(x_j', y_j', 1, \tau_j) = 0, \quad j = 2, 4, \tag{4.4a}$$

$$\frac{\partial W_j'}{\partial z_j}(x_j', y_j', 0, \tau_j) = \frac{\partial W_j'}{\partial z_j}(x_j', y_j', 1, \tau_j) = 0, \quad j = 2, 4, \tag{4.4b}$$

$$\Theta_1'(x_1', y_1', 0, \tau_1) = 0, \tag{4.5a}$$

$$\Theta_5'(x_5', y_5', 1, \tau_5) = 0, \tag{4.5b}$$

$$\Theta_j'(x_j', y_j', 0, \tau_j) \frac{h_j \gamma_j}{h_{j+1} \gamma_{j+1}} = \Theta_{j+1}'(x_{j+1}', y_{j+1}', 1, \tau_{j+1}), \quad j = 1, 2, 3, 4, \tag{4.5c}$$

$$\begin{aligned} \frac{\partial \Theta_{j-1}'}{\partial z_{j-1}'}(x_{j-1}', y_{j-1}', 0, \tau_{j-1}) &= \frac{\partial \Theta_j'}{\partial z_j'}(x_j', y_j', 1, \tau_j) \\ &+ \epsilon_{xz,j} \frac{\partial \Theta_j'}{\partial x_j'}(x_j', y_j', 1, \tau_j) + \epsilon_{yz,j} \frac{\partial \Theta_j'}{\partial y_j'}(x_j', y_j', 1, \tau_j), \quad j = 3, 5, \end{aligned} \tag{4.5d}$$

$$\begin{aligned} \frac{\partial \Theta_{j+1}'}{\partial z_{j+1}'}(x_{j+1}', y_{j+1}', 1, \tau_{j+1}) &= \frac{\partial \Theta_j'}{\partial z_j'}(x_j', y_j', 0, \tau_j) \\ &+ \epsilon_{xz,j} \frac{\partial \Theta_j'}{\partial x_j'}(x_j', y_j', 0, \tau_j) + \epsilon_{yz,j} \frac{\partial \Theta_j'}{\partial y_j'}(x_j', y_j', 0, \tau_j), \quad j = 1, 3, \end{aligned} \tag{4.5e}$$

where $\epsilon_{mn,j} = k_{mn,j}/k_{zz,j}$.

Equations (4.1)–(4.3) with boundary conditions (4.4)–(4.5) constitute a linear homogeneous partial differential equation system. To solve these equations, we

apply a Fourier decomposition to the velocity and temperature disturbances. The base state depends only on the vertical coordinates z_j', so the response to any disturbance will be periodic in the (x', y')-plane and can be expanded in a set of normal modes. The amplitudes of arbitrary temperature and velocity disturbances may be represented as

$$\Theta_j'(x_j', y_j', z_j', \tau_j) = S_j(z_j') \exp[\sigma\tau_j + \mathrm{i}(a_{xj}x_j' + a_{yj}y_j')], \quad j = 1,2,3,4,5,$$

$$W_j'(x_j', y_j', z_j', \tau_j) = U_j(z_j') \exp[\sigma\tau_j + \mathrm{i}(a_{xj}x_j' + a_{yj}y_j')], \quad j = 2,4,$$

where σ is the temporal growth rate, λ is the wavelength common to each layer, and S_j and U_j satisfy

$$(\mathrm{D}_j^2 - a_j^2)(\mathrm{D}_j^2 - a_j^2 - \sigma/Pr_j)\, U_j - a_j^2 Ra_j S_j = 0, \quad j = 2,4, \tag{4.6}$$

$$(\mathrm{D}_j^2 - a_j^2 - \sigma)S_j + U_j = 0, \quad j = 2,4, \tag{4.7}$$

$$\mathrm{D}_j^2 S_j + 2i(a_{xj}\epsilon_{xz,j} + a_{yj}\epsilon_{yz,j})\,\mathrm{D}_j S_j - (\epsilon_{xx,j}a_{xj}^2 + \epsilon_{yy,j}a_{yj}^2 + 2\epsilon_{xy,j}a_{xj}a_{yj})S_j = \sigma S_j, \quad j = 1,3,5, \tag{4.8}$$

subject to the boundary conditions

$$U_j(0) = U_j(1) = \mathrm{D}_j U_j(0) = \mathrm{D}_j U_j(1) = 0, \quad j = 2,4, \tag{4.9}$$

$$S_1(1) = S_5(0) = 0, \tag{4.10}$$

$$S_j(0)\frac{h_j\gamma_j}{h_{j+1}\gamma_{j+1}} = S_{j+1}(1), \quad j = 1,2,3,4, \tag{4.11a}$$

$$\mathrm{D}_1 S_1(0) + \mathrm{i}(\epsilon_{xz,1}a_{x1} + \epsilon_{yz,1}a_{y1})S_1(0) = \mathrm{D}_2 S_2(1), \tag{4.11b}$$

$$\mathrm{D}_3 S_3(1) + \mathrm{i}(\epsilon_{xz,3}a_{x3} + \epsilon_{yz,3}a_{y3})S_3(1) = \mathrm{D}_2 S_2(0), \tag{4.11c}$$

$$\mathrm{D}_3 S_3(0) + \mathrm{i}(\epsilon_{xz,3}a_{x3} + \epsilon_{yz,3}a_{y3})S_3(0) = \mathrm{D}_4 S_4(1), \tag{4.11d}$$

$$\mathrm{D}_5 S_5(1) + \mathrm{i}(\epsilon_{xz,5}a_{x5} + \epsilon_{yz,5}a_{y5})S_5(1) = \mathrm{D}_4 S_4(0), \tag{4.11e}$$

where the total wavevector in layer j is defined as $\boldsymbol{a}_j = a_{xj}\boldsymbol{i} + a_{yj}\boldsymbol{j}$, with magnitude $a_j = (a_{xj}^2 + a_{yj}^2)^{\frac{1}{2}}$, and $\mathrm{D}_j = \mathrm{d}/\mathrm{d}z_j'$.

Since σ depends analytically, and therefore continuously, on the parameters of the problem, the loss of stability must correspond to one or more temporal eigenvalues crossing the imaginary axis and moving from the left half-plane to the right half-plane. In general, the neutral solutions of (4.6)–(4.11) may have $\mathrm{Im}(\sigma) = 0$ (corresponding to steady onset) or $\mathrm{Im}(\sigma) \neq 0$ (corresponding to oscillatory onset).

If it can be shown that only steady onset need be considered, then the 'principle of exchange of stabilities' is said to obtain. To show that only $\mathrm{Im}(\sigma) = 0$ need be considered, it is sufficient to show that for non-negative Ra_2 and Ra_4, all of the neutral solutions correspond to $\mathrm{Im}(\sigma) = 0$.

To proceed, we multiply the energy equation for the jth fluid layer by the conjugate of S_j, multiply the conjugate of the jth energy equation by S_j, and subtract. Similarly, we multiply the momentum equation in layer j by the conjugate of U_j, multiply the conjugate of the jth momentum equation by U_j, and subtract. After eliminating from these two equations terms involving the product of U_j and S_j and their conjugates, we integrate the resulting equation from zero to one. Using the energy equations for the solid walls and the boundary conditions we obtain an equation of the form $\mathrm{Im}(\sigma)[I + J_2 Ra_2 + J_4 Ra_4] = 0$, with I, J_2, and J_4 positive definite, from which it follows that $\mathrm{Im}(\sigma) = 0$ if Ra_2 and Ra_4 are non-negative.

Hence, the momentum and energy equations (4.6)–(4.8) become

$$(\mathrm{D}_j^2 - h_j^2 a_4^2)^2 U_j - h_j^2 a_4^2 \delta_j Ra\, S_j = 0, \quad j = 2, 4, \tag{4.12}$$

$$(\mathrm{D}_j^2 - h_j^2 a_4^2) S_j + U_j = 0, \quad j = 2, 4 \tag{4.13}$$

in the fluid layers. For the solid plates, we have the energy conditions

$$\mathrm{D}_j^2 S_j + 2\mathrm{i}\{h_j a_{x4} \epsilon_{xz,j} + h_j a_{y4} \epsilon_{yz,j}\} \mathrm{D}_j S_j - \{\epsilon_{xx,j} h_j^2 a_{x4}^2 + \epsilon_{yy,j} h_j^2 a_{y4}^2 + 2\epsilon_{xy,j} h_j^2 a_{x4} a_{y4}\} S_j = 0, \quad j = 1, 3, 5. \tag{4.14}$$

The dimensionless quantities δ_j in (4.12) are the ratios

$$\delta_j = Ra_j / Ra, \quad j = 2, 4, \tag{4.15}$$

where Ra is the overall Rayleigh number defined as

$$Ra = \frac{(T_\mathrm{b} - T_\mathrm{u})(L_1 + L_2 + L_3 + L_4 + L_5)^3 \beta_4 g}{\nu_4 \kappa_4}. \tag{4.16}$$

From (4.15) and (4.16), we obtain

$$\delta_4 = \frac{1}{1 + h_1 \gamma_1 + h_2 \gamma_2 + h_3 \gamma_3 + h_5 \gamma_5} \left[\frac{1}{1 + h_1 + h_2 + h_3 + h_5}\right]^3$$

and $\delta_2 = \gamma_2 h_2^4 \Xi \delta_4$, where $\Xi = (\beta_2 \kappa_4 \nu_4)/(\beta_4 \kappa_2 \nu_2)$. We have eliminated all but one wavevector in (4.12)–(4.14) by writing

$$\boldsymbol{a}_j = h_j \boldsymbol{a}_4. \tag{4.17}$$

We note that although the thermal anisotropy of the walls will serve to *orient* the planform, the linear stability analysis still does not *select* the planform (e.g. rolls or hexagons). For the sake of discussion, we shall describe the planform in terms of oriented two-dimensional rolls, with a 'roll angle' defined by

$$\Phi_\mathrm{r} = \tan^{-1}\left[\frac{a_{x4}}{a_{y4}}\right].$$

The solutions of (4.12)–(4.14) subject to (4.9)–(4.11) have eigenvalues $Ra = Ra(\boldsymbol{a}_4)$ with associated disturbances S_j and U_j as eigenfunctions. The eigenvalues Ra depend on Φ_r and the magnitude of $\boldsymbol{a}_4$. In other words, the Rayleigh number is a function of a_{x4} and a_{y4}. The variation of Ra with $\boldsymbol{a}_4$ defines a neutral surface ($\sigma = 0$), on which the minimum value of Ra is defined as the critical Rayleigh number.

5. Solution of the eigenvalue problem

5.1. *Reduction to a coupled pair of matrix eigenvalue problems*

Lienhard (1987) has developed an exact technique for determining the critical Rayleigh number governing the onset of convection in an arbitrary number of horizontal fluid layers separated by thermally isotropic solid walls of arbitrary thickness and conductivity. Taking the bounding plates to be thermally anisotropic considerably increases the complexity of the problem. Therefore, an approximate solution technique will be developed.

Equations (4.12)–(4.14) subject to (4.9)–(4.11) constitute a linear homogeneous system of ordinary differential equations. To solve these equations, we employ a novel Galerkin method.

For the solid plates, the solutions of (4.14) are

$$S_j(z_j') = F_j[\exp(\lambda_{+,j} z_j') + \alpha_j \exp(\lambda_{-,j} z_j')],$$

where

$$\lambda_{\pm,j} = -\mathrm{i}h_j[a_{x4}\epsilon_{xz,j} + a_{y4}\epsilon_{yz,j}] \pm h_j[-(a_{x4}\epsilon_{xz,j} + a_{y4}\epsilon_{yz,j})^2 + (\epsilon_{xx,j}a_{x4}^2 + \epsilon_{yy,j}a_{y4}^2 + 2\epsilon_{xy,j}a_{x4}a_{y4})]^{\frac{1}{2}}$$

and F_j and α_j are constants computed by application of (4.10) and (4.11). From (4.10), we get $\alpha_1 = -\exp(\lambda_{+,1} - \lambda_{-,1})$ and $\alpha_5 = -1$. The other eight thermal boundary conditions (4.11) can be reduced to

$$\mathrm{D}_2 S_2(1) = \Lambda_{z1} S_2(1), \tag{5.1a}$$

$$\mathrm{D}_2 S_2(0) = \Lambda_{z2}(\alpha_3) S_2(0), \tag{5.1b}$$

$$\mathrm{D}_4 S_4(1) = \Lambda_{z3}(\alpha_3) S_4(1), \tag{5.1c}$$

$$\mathrm{D}_4 S_4(0) = \Lambda_{z4} S_4(0), \tag{5.1d}$$

where the coefficients Λ_{z1}, Λ_{z2}, Λ_{z3}, and Λ_{z4} are given in Appendix A.

For the fluid layers, the velocity perturbations U_j, defined on their respective intervals $[0, 1]$, will be expanded in terms of beam functions (Chandrasekhar 1961)

$$U_j(z_j') = \sum_n A_{nj} W_n(z_j') \tag{5.2}$$

which form a complete orthogonal set and satisfy the no-slip condition at the walls.

The even and odd functions are

$$W_n(z') = \frac{\cosh\chi_m(z'-\frac{1}{2})}{\cosh(\frac{1}{2}\chi_m)} - \frac{\cos\chi_m(z'-\frac{1}{2})}{\cos(\frac{1}{2}\chi_m)}, \quad m = \tfrac{1}{2}(n+1), \quad n = 1, 3, 5, \ldots,$$

$$W_n(z') = \frac{\sinh\mu_m(z'-\frac{1}{2})}{\sinh(\frac{1}{2}\mu_m)} - \frac{\sin\mu_m(z'-\frac{1}{2})}{\sin(\frac{1}{2}\mu_m)}, \quad m = \tfrac{1}{2}n, \quad n = 2, 4, 6, \ldots,$$

where χ_m and μ_m satisfy the transcendental equations

$$\tanh\tfrac{1}{2}\chi + \tan\tfrac{1}{2}\chi = 0, \quad \coth\tfrac{1}{2}\mu - \cot\tfrac{1}{2}\mu = 0.$$

The corresponding disturbance temperatures in the fluid layers can be expanded as

$$S_j(z_j') = \sum_n A_{nj} P_{nj}(z_j'), \quad j = 2, 4, \tag{5.3}$$

where each S_j is defined on its respective interval $[0, 1]$, and the functions $P_{nj}(z_j')$ are obtained by solving (4.7) for each $W_n(z_j')$ in (5.2).

We substitute (5.3) into the vertical momentum equations (4.6) to get

$$(\mathrm{D}_j^2 - h_j^2 a_4^2) P_{nj}(z_j') + W_n(z_j') = 0, \quad j = 2, 4. \tag{5.4}$$

Rewriting the boundary conditions by substituting (5.3) into (5.1), we obtain

$$\mathrm{D}_2 P_{n2}(1) = \Lambda_{z1} P_{n2}(1), \tag{5.5a}$$

$$\mathrm{D}_2 P_{n2}(0) = \Lambda_{z2}(\alpha_3) P_{n2}(0), \tag{5.5b}$$

$$\mathrm{D}_4 P_{n4}(1) = \Lambda_{z3}(\alpha_3) P_{n4}(1), \tag{5.5c}$$

$$\mathrm{D}_4 P_{n4}(0) = \Lambda_{z4} P_{n4}(0). \tag{5.5d}$$

The solutions of (5.4) are

$$P_{nj} = \phi_{nj}(z_j') + C'_{nj}\cosh(h_j a_4 z_j') + \mathrm{D}'_{nj}\sinh(h_j a_4 z_j'),$$

where the non-homogeneous part is

$$\phi_{nj}(z_j') = -\frac{\cosh\chi_m(z_j'-\frac{1}{2})}{(\chi_m^2 - h_j^2 a_4^2)\cosh(\frac{1}{2}\chi_m)} - \frac{\cos\chi_m(z_j'-\frac{1}{2})}{(\chi_m^2 + h_j^2 a_4^2)\cos(\frac{1}{2}\chi_m)}, \quad m = \tfrac{1}{2}(n+1), \quad n = 1,3,5,\ldots,$$

$$\phi_{nj}(z_j') = -\frac{\sinh\mu_m(z_j'-\frac{1}{2})}{(\mu_m^2 - h_j^2 a_4^2)\sinh(\frac{1}{2}\mu_m)} - \frac{\sin\mu_m(z_j'-\frac{1}{2})}{(\mu_m^2 + h_j^2 a_4^2)\sin(\frac{1}{2}\mu_m)}, \quad m = \tfrac{1}{2}n, \quad n = 2,4,6,\ldots.$$

The disturbance temperature functions $P_{nj}(z_j')$ are chosen to satisfy the boundary conditions (5.5*a–d*). Substituting (5.2) and (5.3) for each layer into the momentum equation (4.6), multiplying by W_m, and integrating from 0 to 1, we obtain a matrix eigenvalue problem

$$[\boldsymbol{C}_j(Ra) - \alpha_3 \boldsymbol{B}_j(Ra)]\boldsymbol{A}_j = 0, \quad j = 2,4 \tag{5.6}$$

for each fluid layer, where the elements of the matrices $\boldsymbol{B}_j$ and $\boldsymbol{C}_j$ are given by

$$B_j(m,n) = -X_{j1}(m,n) + Ra\,X_{j2}(m,n),$$

$$C_j(m,n) = Y_{j1}(m,n) - Ra\,Y_{j2}(m,n),$$

the elements of $\boldsymbol{X}$ and $\boldsymbol{Y}$ are defined in Appendix B, and $\boldsymbol{A}_j$ is a vector of coefficients (cf. (5.2)) in the jth layer.

5.2. *Solution of the coupled matrix eigenvalue problems*

For arbitrarily chosen values of the wavevector magnitude in the fourth fluid layer (a_4) and the roll angle (Φ_r), we compute $\boldsymbol{a}_j$ from (4.17) with components $a_{xj} = a_j\cos\Phi_r$ and $a_{yj} = a_j\sin\Phi_r$. The unknown parameters α_3 and Ra appear linearly in (5.6). To compute Ra for a given wavevector $\boldsymbol{a}_4$, we could guess an initial value of Ra, and compute the sets of eigenvalues α_3 of (5.6) for $j = 2$ and 4. We could then iterate on Ra until the two eigenvalue problems have a common eigenvalue. For a given $\boldsymbol{a}_4$, we would then have a point on the neutral surface.

This procedure was implemented in a computer code. Unfortunately, it was rather expensive, so a more efficient technique was developed. We begin with a general outline of the procedure. Given the linear dependence of each matrix element in (5.6) on α_3 and Ra, we can write the determinantal polynomial for each j as

$$0 = |\boldsymbol{C}_j(Ra) - \alpha_3 \boldsymbol{B}_j(Ra)| = \prod_{m=1}^{N} [\omega_{mj}(Ra, \boldsymbol{a}_4) - \alpha_3 \zeta_{mj}(Ra, \boldsymbol{a}_4)], \quad j = 2,4, \tag{5.7}$$

where ω_{mj} and ζ_{mj} are polynomials in Ra. On the basis of extensive numerical experimentation, it is clear that in (5.6) only one eigenvalue α_3 in each case ($j = 2,4$) depends on Ra and $\boldsymbol{a}_4$. The others are identical and independent of Ra and $\boldsymbol{a}_4$ to within machine precision. Thus, we can write (5.7) as

$$Q_{Nj}(Ra, \boldsymbol{a}_4, \alpha_3) \equiv (H_j - \alpha_3)^{N-1}[\omega_{Nj}(Ra, \boldsymbol{a}_4) - \alpha_3 \zeta_{Nj}(Ra, \boldsymbol{a}_4)] = 0, \quad j = 2,4, \tag{5.8}$$

where, for $j = 2$ and 4, H_j are eigenvalues of (5.6) having algebraic multiplicities of $N-1$ and which do not depend on Ra and $\boldsymbol{a}_4$. We then regard (5.8) as a pair of polynomial equations in α_3 and Ra, from which α_3 may be eliminated. The resulting equation in Ra is of polynomial type, and is easily solved using standard numerical techniques. The details of the above procedure are as follows.

We fix Ra, compute eigenvalues α_3 of the matrix eigenvalue problems (5.6) for $j = 2, 4$ and note the constant eigenvalues H_2 and H_4. We arbitrarily choose α_3. The determinant $|\boldsymbol{C}_j - \alpha_3 \boldsymbol{B}_j|$ is evaluated at N values of Ra, and its characteristic polynomial is computed using the technique of Pacagnella & Pierobon (1975). The N values of Ra required in the latter procedure are chosen as

$$Ra_m = \exp\left[\frac{2(m-1)\,\pi \mathrm{i}}{N+1}\right], \quad 1 \leqslant m \leqslant N.$$

We then write Q_{Nj} as

$$Q_{Nj}(Ra, \alpha_{3,k}) = \sum_{m=0}^{N} r_{k,m} Ra^m,$$

where the $r_{k,m}$ are constants. For two arbitrarily selected values of α_3, we have

$$\omega_{Nj}(Ra) - \alpha_{3,k}\,\zeta_{Nj}(Ra) = \frac{1}{(H_j - \alpha_{3,k})^{N-1}} \sum_{m=0}^{N} r_{k,m} Ra^m, \quad k = 1, 2. \tag{5.9}$$

From (5.9), for $k = 1, 2$, we compute ω_{Nj} and ζ_{Nj} and use (5.8) to obtain

$$\alpha_3 = \frac{\omega_{Nj}(Ra)}{\zeta_{Nj}(Ra)}, \quad j = 2, 4.$$

On the neutral surface, α_3 must be the same in (5.6) for $j = 2$ and 4, from which fact we obtain a single equation in Ra:

$$\frac{\omega_{N2}(Ra)}{\zeta_{N2}(Ra)} = \frac{\omega_{N4}(Ra)}{\zeta_{N4}(Ra)}. \tag{5.10}$$

To determine the Rayleigh number on the neutral surface we rewrite (5.10) as a polynomial equation, which is solved by a standard technique (Jenkins & Traub 1972).

Our main interest is to minimize Ra as a function of $\boldsymbol{a}_4$, since this gives the Ra at which the multilayered system first becomes linearly unstable. To locate the minimum of $Ra\,(\boldsymbol{a}_4)$, we first note that, because of symmetry, one need only consider Φ_r in the range $0 \leqslant \Phi_r \leqslant \pi$ (or any other half of the wavevector plane). We then find the minimum value of Ra as a function of a_4 for $K+1$ evenly spaced values of Φ_r. This is accomplished using a three-point iteration scheme. For each Φ_r, we first compute neutral values of Ra at three values of a_4 (an initial guess is made for a_4; the second and third values are chosen by decreasing and increasing the initial value by 2.5%). A parabola $Ra_p = u_0 + u_1 a_4 + u_2 a_4^2$ is fitted to these three points, and subsequent iterates are obtained by setting $\mathrm{d}Ra_p/\mathrm{d}a_4 = 0$. The three values of a_4 are updated and the iteration is continued until the relative change in a_4 at the minimum is less than 10^{-4}. This minimization process is performed for the $K+1$ values of Φ_r. The smallest of these Rayleigh numbers, and the wavenumber $a_{4,\min}$ and roll angle $\Phi_{r,\min}$ at which this Ra occurs are noted. We then fix $a_4 = a_{4,\min}$, and compute the Rayleigh numbers at $M+1$ equidistant values of Φ_r in the range $[\Phi_{r,\min} - \Delta\Phi_r \leqslant \Phi_r \leqslant \Phi_{r,\min} + \Delta\Phi_r]$, where $\Delta\Phi_r = \pi/K$. We next select the smallest of these Rayleigh numbers and its associated Φ_r. We then fix the roll angle, and continue this 'alternating direction' iteration until the relative changes in Ra, a_4, and Φ_r are less than 10^{-7}, 10^{-6}, and 10^{-5}, respectively.

6. Results

When the solid boundaries are isotropic, the Rayleigh number depends only on the magnitude of the wavevector. Thus, the neutral surface is axisymmetric about $a_4 = 0$ and the relation $Ra = Ra(a_4)$ defines a neutral curve. However, for thermally anisotropic solid boundaries, the Rayleigh number is a function of both the magnitude of the wavevector and the planform orientation, as expressed through the roll angle. Figure 2 displays a typical neutral surface for highly anisotropic solid boundaries.

Consideration will now be given to how the planform orientation depends on plate orientation. In what follows, we have chosen $\epsilon_{xz,i} = \epsilon_{yz,i} = 0$ $(i = 1, 3, 5)$ so that the thermal conductivity tensor of each plate can be rendered orthotropic by rotation about the z-axis. We define a 'plate angle' Φ_p in terms of the angle between the principal axes of the conductivity tensors of the middle and top plates. A plate angle of 0° corresponds to the situation in which the largest components of the conductivity tensor of the middle and top plates are aligned.

The plate materials initially considered are graphite fibre epoxy for layers one and five, and pyrolytic graphite in the middle. Both materials are transversely isotropic, with thermal conductivity ratios $(k_\parallel/k_\perp)$ of 12.76 and 342.1, respectively. Here, $k_\parallel$ and $k_\perp$ are the thermal conductivities in planes parallel and perpendicular, respectively, to the plane in which the conductivity is isotropic. For both fluid layers, we select water with the reference temperature taken as 15 °C. With the conductivity ratios γ_1, γ_2, γ_3, and γ_5 thus specified, we fix the thickness ratios h_1, h_2, and h_5, and vary the thickness ratio h_3 of the middle plate.

For $h_1 = h_5 = 0.25$, attention will first be directed to the case $h_2 = 0.01$. The roll angle as a function of (the middle layer) plate angle is shown in figure 3 for various values of h_3. As h_3 is varied, the topology of the Φ_r–Φ_p plots changes. In figure 3(*a*), for $h_3 = 2.5 \times 10^{-4}$, there is an almost sinusoidal variation of the roll angle with plate angle. We note that, in general, the roll orientation may be expected to depend on the anisotropy of the three solid plates in a fairly complicated, nonlinear fashion. In this first case, the middle plate is very thin. Therefore, of the terms involving the thermal anisotropy of the middle plate, only the first-order (i.e. linear) terms affect the planform orientation. Owing to the thinness of the middle plate, Φ_r is primarily determined by the outer plates. Thus, the effect of varying Φ_p is to apply a weak modulation to the constant value of Φ_r which, for an isotropic middle plate, would be determined by the alignment of the top and bottom plates. As the middle-plate thickness increases (figure 3*b*), the sinusoidal variation of Φ_r becomes distorted owing to the effects of higher-order terms in the relationship between Φ_r and the properties and orientation of the middle plate. Finally, we note that Φ_r is a π-periodic function of Φ_p, owing to the 180° ambiguity in the definition of the orientation of a set of two-dimensional rolls.

A three-dimensional plot of the neutral surface (Ra as a function of $\boldsymbol{a}_4$) is shown in figure 4 for $h_3 = 1.007\,812\,5 \times 10^{-3}$. We see that the surface has two local minima. As the thickness of the middle plate increases, a 'crossover' of these two minima occurs, in which the global minimum shifts from one local minimum to the other. The Φ_r–Φ_p plot shows two discontinuities in each π-period, each of which corresponds to a switching of the global minimum on the Ra–$\boldsymbol{a}_4$ surface between two local minima. There are four branches in a 2π-period. As h_3 is increased further, two of the branches shrink (figure 3*d*) and ultimately merge with the other two branches (figure 3*e*). Note that any of the four branches may in its entirety be shifted up or down by 180°,

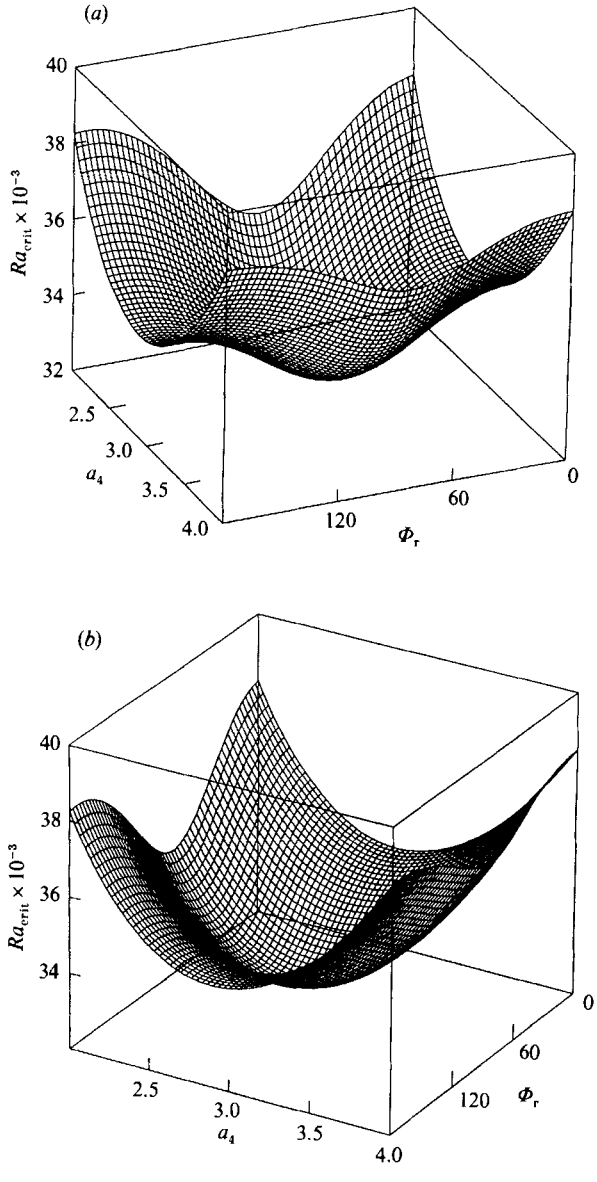

FIGURE 2. Typical neutral surface for highly anisotropic solid boundaries for $h_1 = 0.25$, $h_2 = 0.5$, $h_3 = 0.15$, $h_5 = 0.4$, $\gamma_1 = 0.6$, $\gamma_2 = 1$, $\gamma_3 = 0.2$, $\gamma_5 = 0.65$, $\epsilon_{xx,1} = 2.759$, $\epsilon_{zz,1} = 0.9$, $\epsilon_{yz,1} = 0.8$, $\epsilon_{xy,1} = 0.75$, $\epsilon_{yy,1} = 0.5$, $\epsilon_{xz,3} = 1.6$, $\epsilon_{xz,3} = 0.35$, $\epsilon_{yz,3} = 0.6$, $\epsilon_{xy,3} = 0$, $\epsilon_{yy,3} = 0.8$, $\epsilon_{xx,5} = 1.759$, $\epsilon_{zz,5} = 0.45$, $\epsilon_{yz,5} = 0.7$, $\epsilon_{xy,5} = 0.45$, $\epsilon_{yy,5} = 0.7$, $\Xi = 1$: (a, b) show the same surface from two different views.

owing to the previously discussed 180° ambiguity. Thus, at the value of h_3 at which two of the branches disappear, the remaining two branches can be plotted separately with two jumps, or as the smooth curve shown in figure 3(*e*). When the middle plate is very thick, it exerts a very strong influence on the roll angle. In that case, Φ_r is said to be *slaved* to Φ_p (figure 3*f*).

The situation is somewhat different for $h_2 = 1$, as shown in figure 5. The two limiting cases, when the middle plate is very thin (figure 5*a*) or very thick (figure 5*f*),

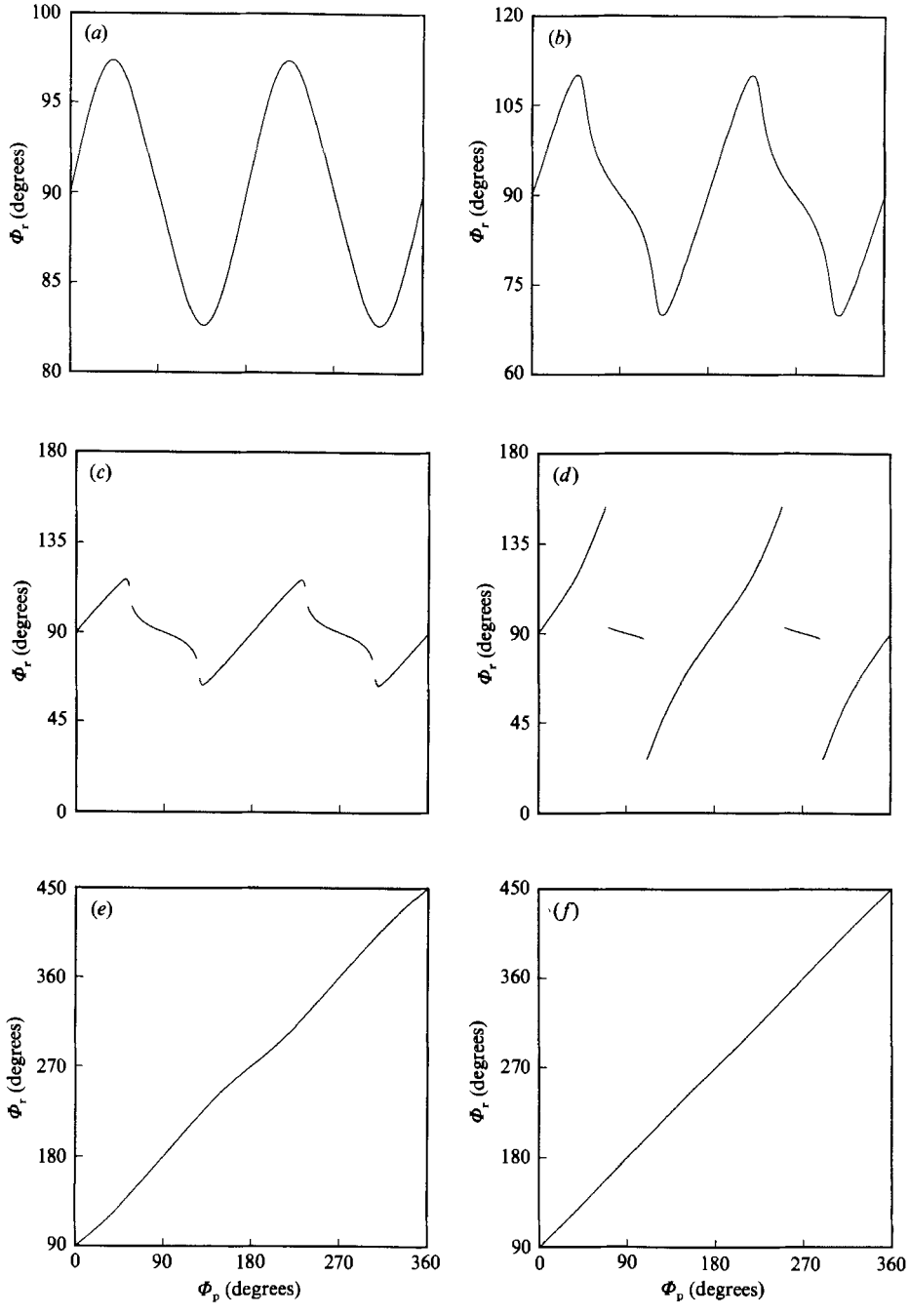

FIGURE 3. Φ_r–Φ_p plots for various h_3 for $h_1 = 0.25$, $h_2 = 0.01$, $h_5 = 0.25$, $\gamma_1 = 0.699$, $\gamma_2 = 1$, $\gamma_3 = 0.107$, $\gamma_5 = 0.699$, $\Xi = 1$. The top and bottom plates are graphite fibre epoxy with $\epsilon_{xx,1} = \epsilon_{xx,5} = 12.76$, $\epsilon_{yy,1} = \epsilon_{yy,5} = 1$, $\epsilon_{xy,1} = \epsilon_{xy,5} = 0$, $\epsilon_{xz,1} = \epsilon_{xz,5} = 0$, $\epsilon_{yz,1} = \epsilon_{yz,5} = 0$. The middle plate is pyrolytic graphite. For $\Phi_p = 0°$, $\epsilon_{xx,3} = 342.1$, $\epsilon_{yy,3} = 1$, $\epsilon_{xy,3} = \epsilon_{xz,3} = \epsilon_{yz,3} = 0$. (*a*) $h_3 = 2.5 \times 10^{-4}$, (*b*) 8.1835937×10^{-4}, (*c*) 1.0078125×10^{-3}, (*d*) 1.765625×10^{-3}, (*e*) 3.28125×10^{-3}, (*f*) 1.2375×10^{-2}.

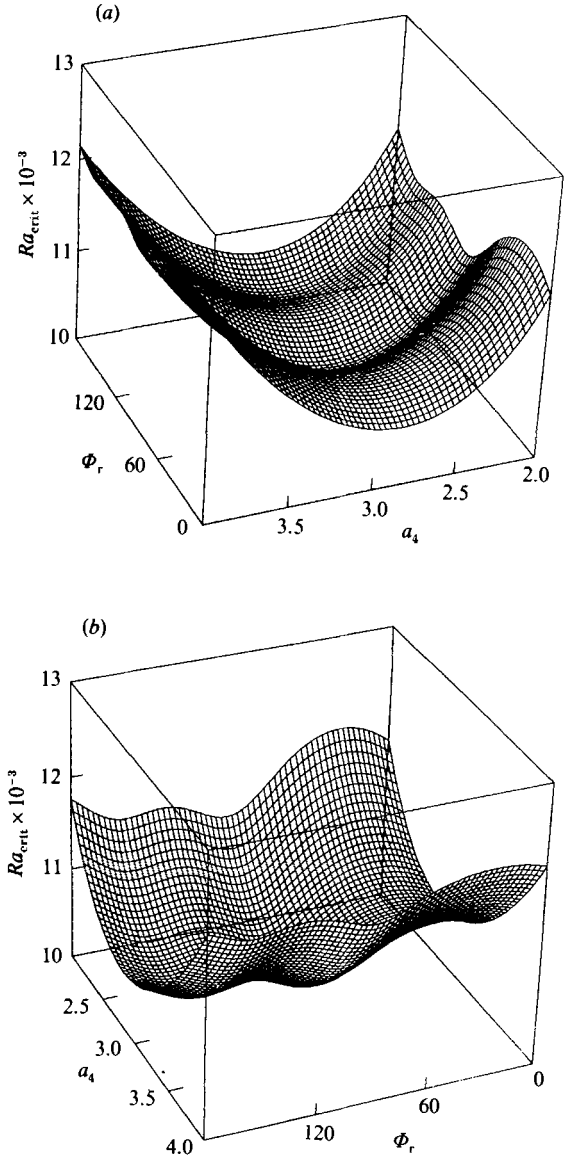

FIGURE 4. Ra–a_4 neutral surface for $\Phi_p = 69°$, $h_1 = 0.25$, $h_2 = 0.01$, $h_3 = 1.0078125 \times 10^{-3}$, $h_5 = 0.25$, $\gamma_1 = 0.699$, $\gamma_2 = 1$, $\gamma_3 = 0.107$, $\gamma_5 = 0.699$, $\Xi = 1$. Plate materials are as in figure 3. The maximum conductivities of the top and bottom plates are in the direction of the x-axis. (a, b) show the same neutral surface from two different views.

are the same as for smaller h_2. However, in the range of h_3 for which the Φ_r–Φ_p plot is discontinuous, the roll angle on the branches which ultimately disappear is near 0° (or 180°) for $h_2 = 1$ instead of near 90° as for smaller h_2.

Other calculations were conducted and the results are presented in figure 6 for a different configuration. Here, we select pyrolytic graphite for the outer plates, graphite fibre epoxy for the middle plate, and water for both fluid layers. For sufficiently large h_3, Φ_r is again slaved to Φ_p (figure 6a). As h_3 decreases, Φ_r remains slaved to Φ_p, except near $\Phi_p = 0° = 360°$ and 180°, where Φ_p has a minor influence

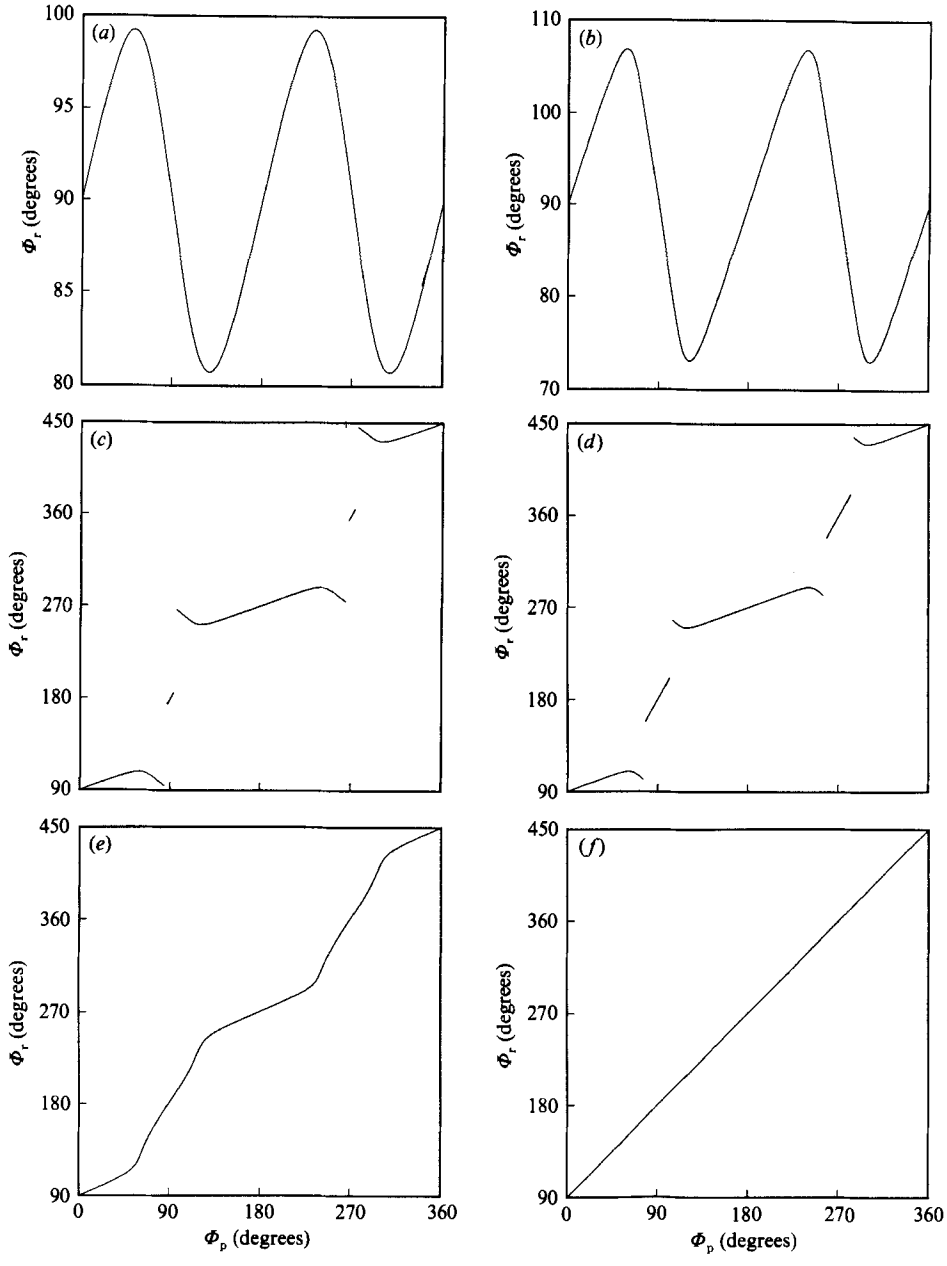

FIGURE 5. Φ_r–Φ_p plots for various h_3 for $h_2 = 1$. All other parameters are as in figure 3. (*a*) $h_3 = 2.5 \times 10^{-6}$, (*b*) 4.0625×10^{-5}, (*c*) $4.258\,125 \times 10^{-5}$, (*d*) $4.843\,75 \times 10^{-5}$, (*e*) 5.625×10^{-5}, (*f*) 2.5×10^{-3}.

on Φ_r, which is primarily determined by the orientation of the top and bottom plates. Decreasing h_3 further leads to a broadening of the region in which Φ_r is relatively independent of Φ_p. At a critical value of h_3, a discontinuity appears, as shown in figure 6(*c*). Again, there are four branches in each 2π-period. The two which are remnants of the original (large h_3) curve will be referred to as the slaved branches. The other two (approximately) constant branches are at approximately $\Phi_r = 270°$

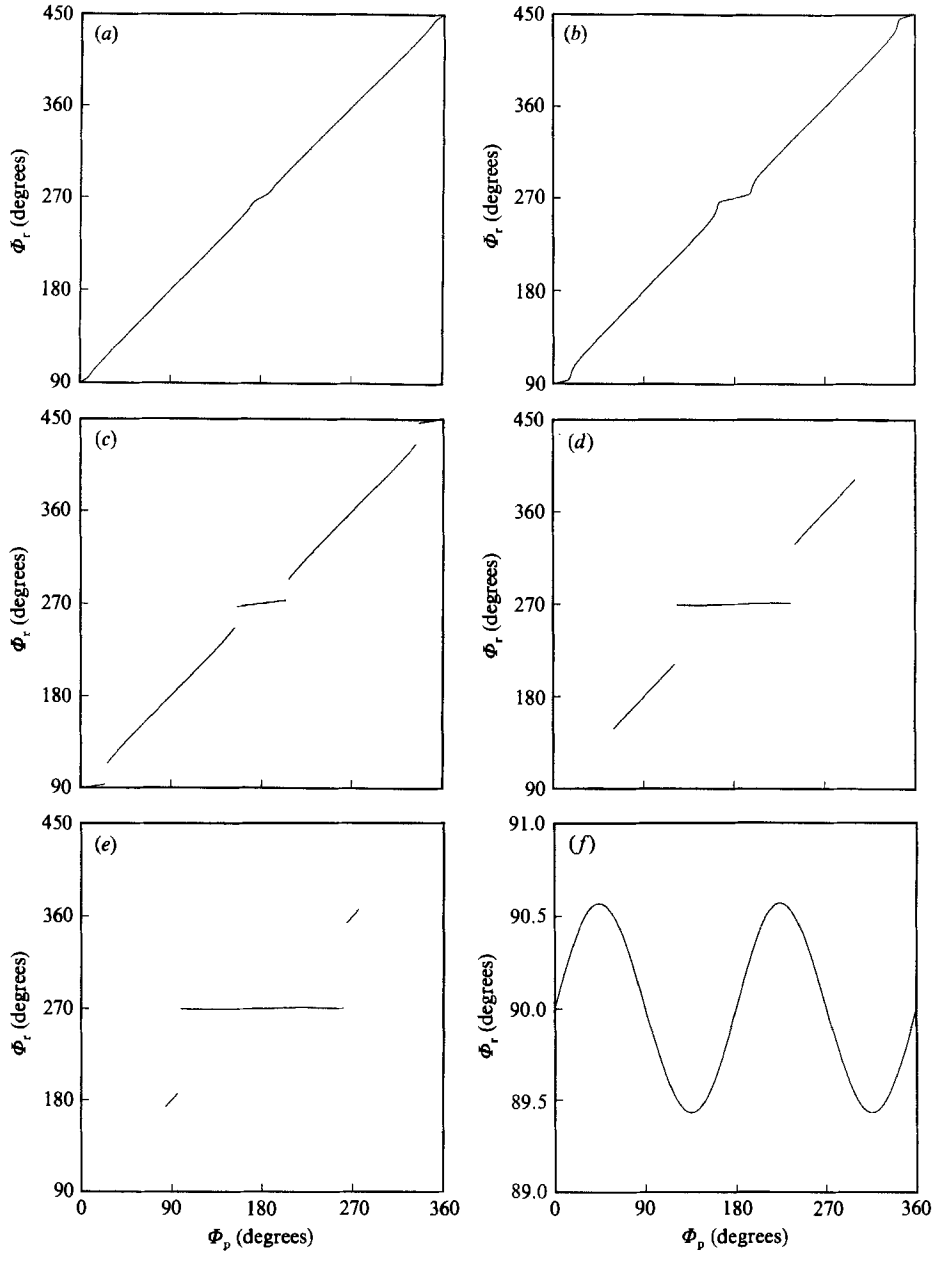

FIGURE 6. Φ_r–Φ_p plots for various h_3 for $h_1 = 0.25$, $h_2 = 1$, $h_5 = 0.25$, $\gamma_1 = 0.107$, $\gamma_2 = 1$, $\gamma_3 = 0.699$, $\gamma_5 = 0.107$, $\Xi = 1$. The top and bottom plates are pyrolytic graphite with $\epsilon_{xx,1} = \epsilon_{xx,5} = 342.1$, $\epsilon_{yy,1} = \epsilon_{yy,5} = 1$, $\epsilon_{xy,1} = \epsilon_{xy,5} = 0$, $\epsilon_{xz,1} = \epsilon_{xz,5} = 0$, $\epsilon_{yz,1} = \epsilon_{yz,5} = 0$. The middle plate is graphite fibre epoxy. For $\Phi_p = 0°$, $\epsilon_{xx,3} = 12.76$, $\epsilon_{yy,3} = 1$, $\epsilon_{xy,3} = \epsilon_{xz,3} = \epsilon_{yz,3} = 0$. (*a*) $h_3 = 2.5 \times 10^{-1}$, (*b*) $3.343\,75 \times 10^{-2}$, (*c*) $1.796\,875 \times 10^{-2}$, (*d*) $4.438\,593\,75 \times 10^{-3}$, (*e*) $3.287\,553\,71 \times 10^{-3}$, (*f*) 2.5×10^{-3}.

(for Φ_p in the vicinity of 180°) and at 90° (= 450°) for Φ_p near 0° (= 360°). As h_3 is further reduced, the region in which Φ_r is determined by the outer plates grows, as does the magnitude of the jump in Φ_r at the discontinuity. When h_3 is very small, we reach the other limiting case in which the slaved branches disappear completely and Φ_r is primarily determined by the outer plates for all values of Φ_p.

We observe that the middle plate sometimes exerts a much stronger influence on the planform orientation than do the top and bottom plates. Figure 6(*a*) shows that when the thicknesses of all three plates are equal, and the top and bottom (pyrolytic graphite) plates are much more anisotropic than the middle (graphite fibre epoxy) plate, Φ_r is completely slaved to Φ_p. Figure 6(*b*) shows that, when the thickness of the middle plate is drastically reduced, the orientation of the middle plate still controls Φ_r for almost all values of Φ_p.

Figure 7 shows Φ_r as a function of Φ_p for various values of h_3. In this case, all three plates are of the same material, with the top and bottom plates oriented in the same direction. When h_3 is sufficiently large, Φ_r is slaved to Φ_p, as usual. For smaller h_3, Φ_r is modulated slightly about the linear dependence on Φ_p, as shown in figure 7(*a*). As h_3 decreases, the departure from linearity increases, and the approximately *piecewise* linear dependence of Φ_r on Φ_p shown in figures 7(*b*) and 7(*c*) develops. The sharp changes in slope which occur at 90° and 270° become discontinuities as h_3 is decreased still further, as shown in figure 7(*d*). In this case, the Φ_r–Φ_p plot has two branches. For still smaller values of h_3 another discontinuity develops, yielding the four-branch Φ_r–Φ_p plot shown in figure 7(*e*). Further decreases in h_3 lead to the development of additional discontinuities, as exhibited by the eight-branch Φ_r–Φ_p plot shown in figures 7(*f*) and 7(*g*) (which shows the details of the range of Φ_p in which the additional branches develop). When h_3 is reduced further, the discontinuities eventually disappear (figure 7*h*) and the limiting case of small sinusoidal variation of Φ_r about 90° is reached (figure 7*i*).

We also consider the case in which the directions of maximum conductivity in the top and bottom plates differ by 90°. In this situation, the limiting case for very small h_3 is not an approximately sinusoidal variation of Φ_r about 90°, but is almost piecewise constant, with four branches near $\Phi_r = 90°$, 180°, 270°, and 360° (= 0°), as shown in figure 8(*a*). From figure 8 and the numerical results, it is seen that the discontinuities always occur at $\Phi_p = 45°$ and 135°. Since the top and bottom plates have the same thickness, and the middle plate is very thin, the roll orientation is basically determined by the top plate for $-45° \leqslant \Phi_p \leqslant 45°$, and varies, with small amplitude, about 90°. In the range $45° \leqslant \Phi_p \leqslant 135°$, the bottom plate determines the planform orientation, with Φ_r varying about 180°. We thus see that, centred about 90°, 180°, 270°, and 360°, there are 90° bands of Φ_p for which Φ_r is almost constant and determined by the orientation of either the top or bottom plate. As h_3 increases, the discontinuity in Φ_r decreases and the variation along each branch increases. When h_3 is increased further, the discontinuities eventually disappear, as shown in figure 8(*d*). For h_3 sufficiently large, the middle plate determines the planform orientation, and Φ_r is slaved to Φ_p.

Consideration will now be given to how the limiting case of very small h_3 is affected by the relative orientation of the top and bottom plates. We consider the situation in which all three plates are made of the same material. For very small h_3, the limiting case of almost sinusoidal variation of Φ_r about 90° was shown in figure 7(*a*) when the top and bottom plates were identically oriented. In figure 8(*a*), the limiting case of Φ_r being almost piecewise constant about 90°, 180°, 270°, 360° was shown for the case in which the directions of maximum conductivities of the top and bottom plates differed by 90°. Now we fix the thickness of the middle plate ($h_3 = 4 \times 10^{-4}$), and present results in figure 9 for different orientations of the bottom plate with respect to the top plate. First we consider the case in which the angle ($\Delta\Phi$) between the directions of maximum conductivities of the top and bottom plates is 10°. The limiting case of small $\Delta\Phi$ is one of small, almost sinusoidal variation of Φ_r about 95°,

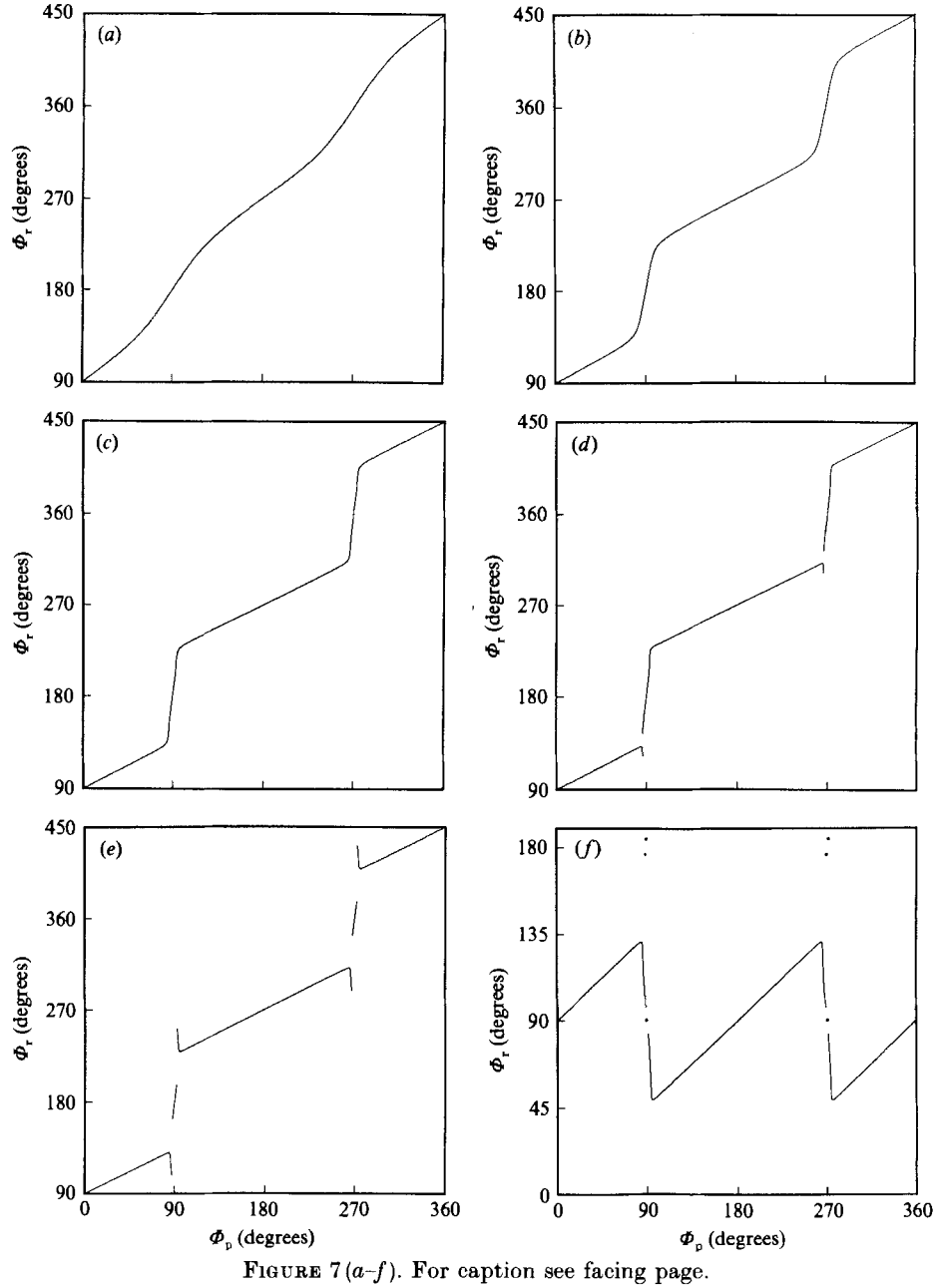

FIGURE 7 (*a–f*). For caption see facing page.

as shown in figure 9(*a*). This is a 90° shift from one-half the sum of the angles (0° and 10°) associated with the directions of maximum conductivity of the top and bottom plates. As $\Delta\Phi$ increases, the amplitude of the variation increases, as shown in figures 9(*b*) and 9(*c*) for $\Delta\Phi = 80°$ and 83°, respectively. As $\Delta\Phi$ increases further, one discontinuity in each π-period develops, as shown in the two-branch Φ_r–Φ_p plot of figure 9(*d*). When $\Delta\Phi$ is increased still further, another discontinuity develops, which yields the four-branch Φ_r–Φ_p plot shown in figure 9(*e*). For larger values of $\Delta\Phi$, the variation on each branch gets smaller and the jump gets larger, as shown in figures

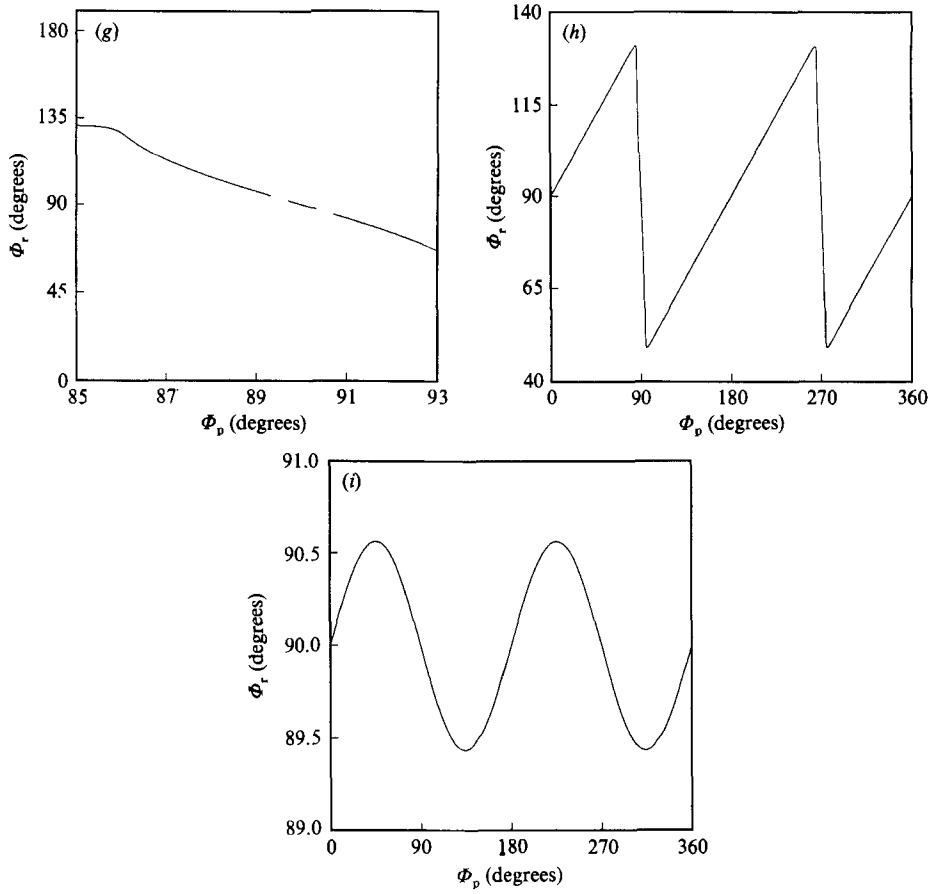

FIGURE 7. Φ_r–Φ_p plots for various h_3 for $h_1 = 0.8$, $h_2 = 1$, $h_5 = 0.8$, $\gamma_1 = 5$, $\gamma_2 = 1$, $\gamma_3 = 5$, $\gamma_5 = 5$, $\Xi = 1$. All plates are made of the same material. The top and bottom plates are aligned with their maximum conductivities in the direction of the x-axis with $\epsilon_{xx,1} = \epsilon_{xx,5} = 0.95$, $\epsilon_{yy,1} = \epsilon_{yy,5} = 0.25$, $\epsilon_{xy,1} = \epsilon_{xy,5} = 0$, $\epsilon_{xz,1} = \epsilon_{xz,5} = 0$, $\epsilon_{yz,1} = \epsilon_{yz,5} = 0$. For $\Phi_p = 0°$, $\epsilon_{xx,3} = 0.95$, $\epsilon_{yy,3} = 0.25$, $\epsilon_{xy,3} = \epsilon_{xz,3} = \epsilon_{yz,3} = 0$. (*a*) $h_3 = 1.2$, (*b*) 4.4×10^{-1}, (*c*) 4.0625×10^{-1}, (*d*) $4.027\,343\,75 \times 10^{-1}$, (*e*) $4.023\,828\,125 \times 10^{-1}$, (*f*) $4.022\,509\,766 \times 10^{-1}$, (*g*) enlarged version of (*f*), (*h*) $h_3 = 4.022\,290\,039 \times 10^{-1}$, (*i*) 8×10^{-3}.

9(*f*) and 9(*g*). As $\Delta\Phi$ is increased to 90°, the limiting case of almost piecewise constant Φ_r variation about 90°, 180°, 270°, and 360° is reached.

To complete the presentation of our results, we consider two more cases in which layers two and four are occupied by different fluids. In each case, the fluids considered are silicone oil in the second layer and water in the fourth.

In one case, the top and bottom plates are graphite fibre epoxy, and the middle plate is pyrolytic graphite. The results are presented in figure 10 for fixed values of all the thickness ratios except h_3, which is varied. We obtain essentially the same sequence of Φ_r–Φ_p plots as was shown in figure 3, when both fluid layers were water.

In the other case, the top and middle plates are made of graphite fibre epoxy, and the bottom plate is pyrolytic graphite. We again fix all parameters except the middle plate thickness ratio h_3 and present the results in figure 11 for different values of h_3. The results are very similar to those obtained for the cases shown in figure 5.

The results depend on 24 dimensionless parameters, so that a complete exploration of the parameter space is not feasible.

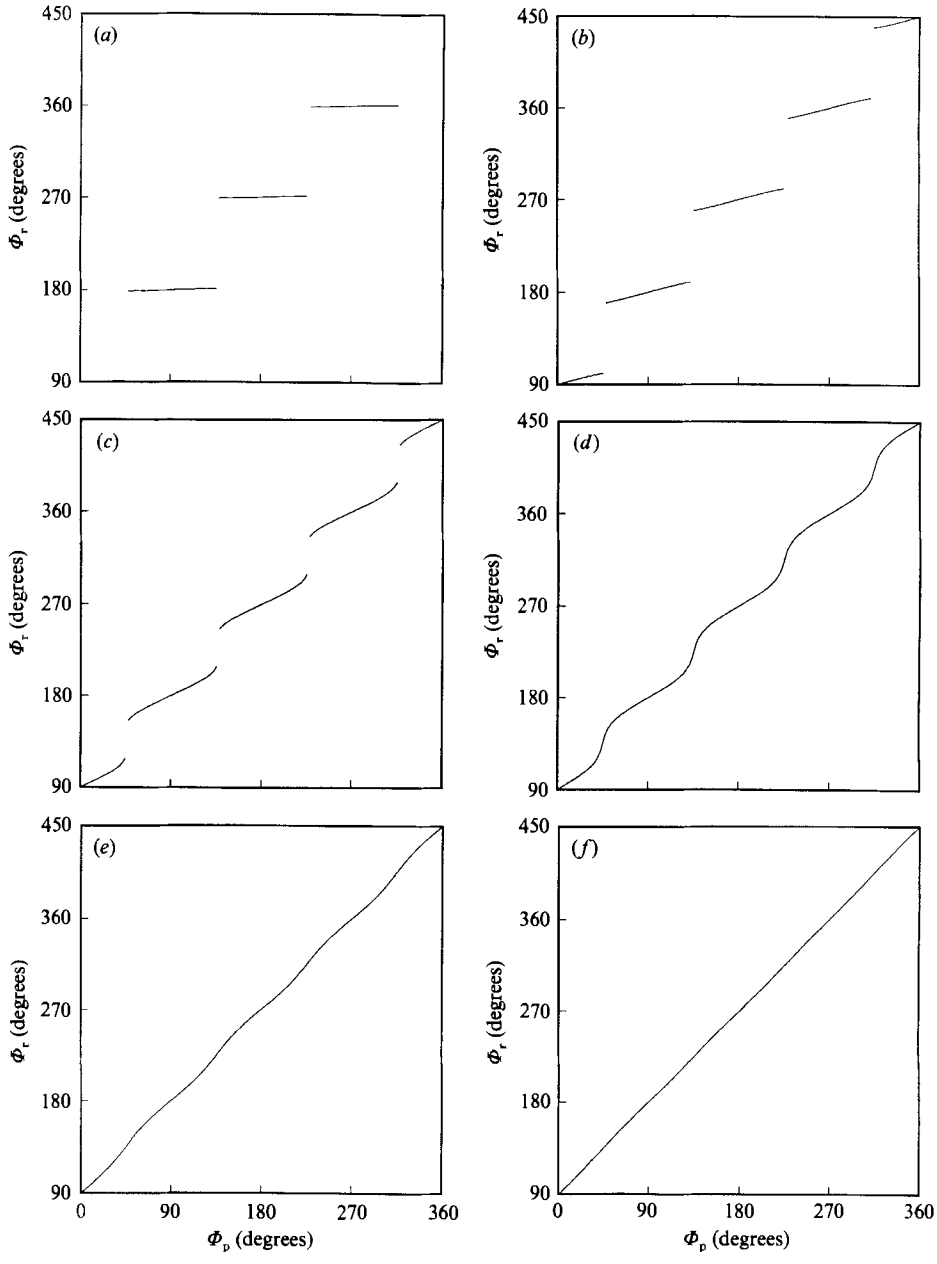

FIGURE 8. Φ_r–Φ_p plots for various h_3 for $h_1 = 0.4$, $h_2 = 1$, $h_5 = 0.4$, $\gamma_1 = 2$, $\gamma_2 = 1$, $\gamma_3 = 2$, $\gamma_5 = 2$, $\Xi = 1$. Plate materials are as in figure 7. The maximum conductivities of the top and bottom plates are aligned with the x- and y-axes, respectively. For $\Phi_p = 0°$, $\epsilon_{xx,3} = 0.95$, $\epsilon_{yy,3} = 0.25$, $\epsilon_{xy,3} = \epsilon_{xz,3} = \epsilon_{yz,3} = 0$. (*a*) $h_3 = 4 \times 10^{-4}$, (*b*) 4×10^{-3}, (*c*) 9.2875×10^{-3}, (*d*) 1.4575×10^{-2}, (*e*) 5.35×10^{-2}, (*f*) 4×10^{-1}.

FIGURE 9. Φ_r–Φ_p plots for various $\Delta\Phi$ (the angle between the directions of maximum conductivities of the top and bottom plates) for $h_1 = 0.4$, $h_2 = 1$, $h_3 = 4 \times 10^{-4}$, $h_5 = 0.4$, $\gamma_1 = 2$, $\gamma_2 = 1$, $\gamma_3 = 2$, $\gamma_5 = 2$, $\Xi = 1$. Plate materials are as in figure 7. The maximum conductivity of the top plate is in the direction of the x-axis. For $\Phi_p = 0°$, $\epsilon_{xx,3} = 0.95$, $\epsilon_{yy,3} = 0.25$, $\epsilon_{xy,3} = \epsilon_{xz,3} = \epsilon_{yz,3} = 0$. (*a*) $\Delta\Phi = 10°$, (*b*) 80°, (*c*) 83°, (*d*) 84°, (*e*) 84.5°, (*f*) 85°, (*g*) 87.5°.

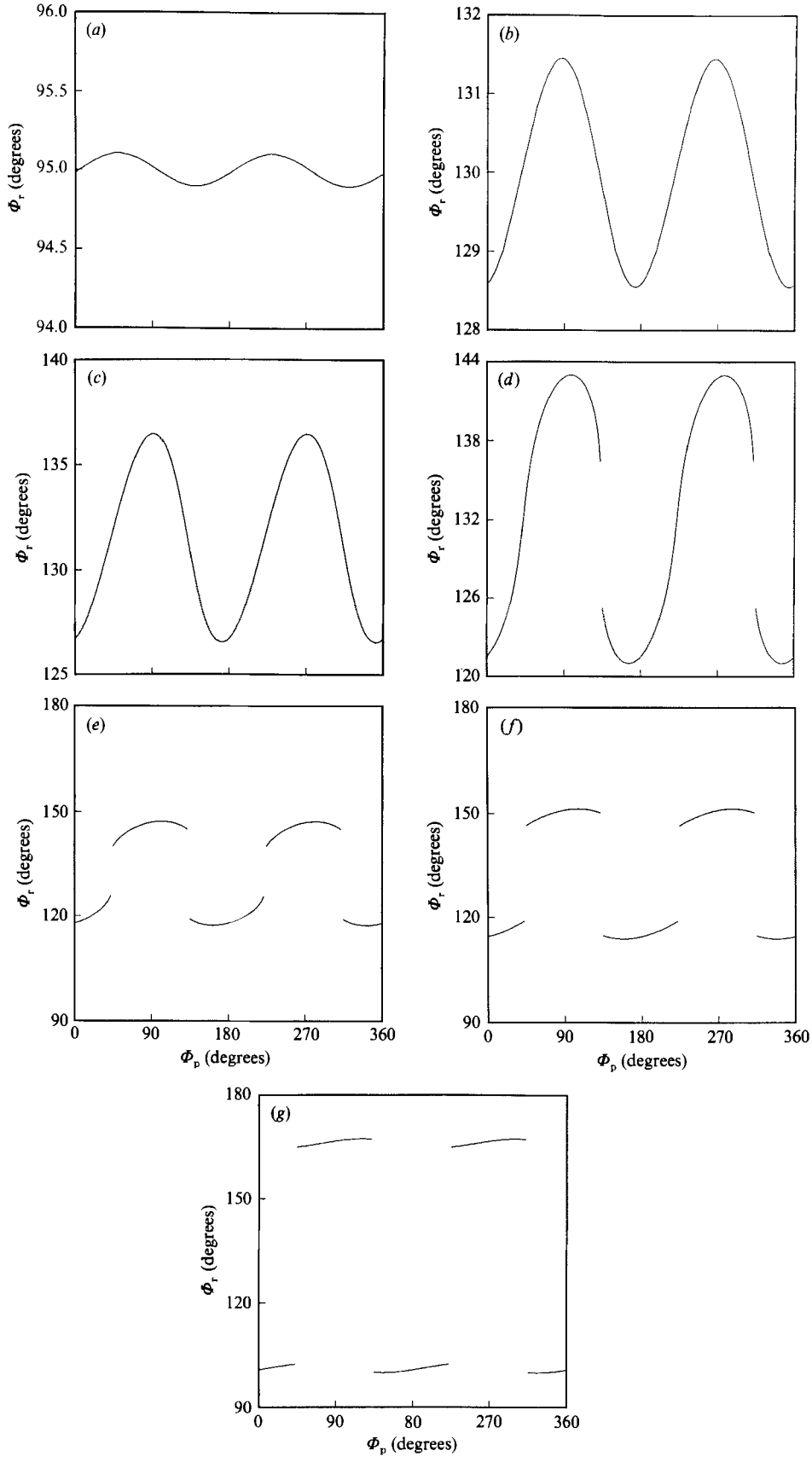

FIGURE 9(*a–g*). For caption see facing page.

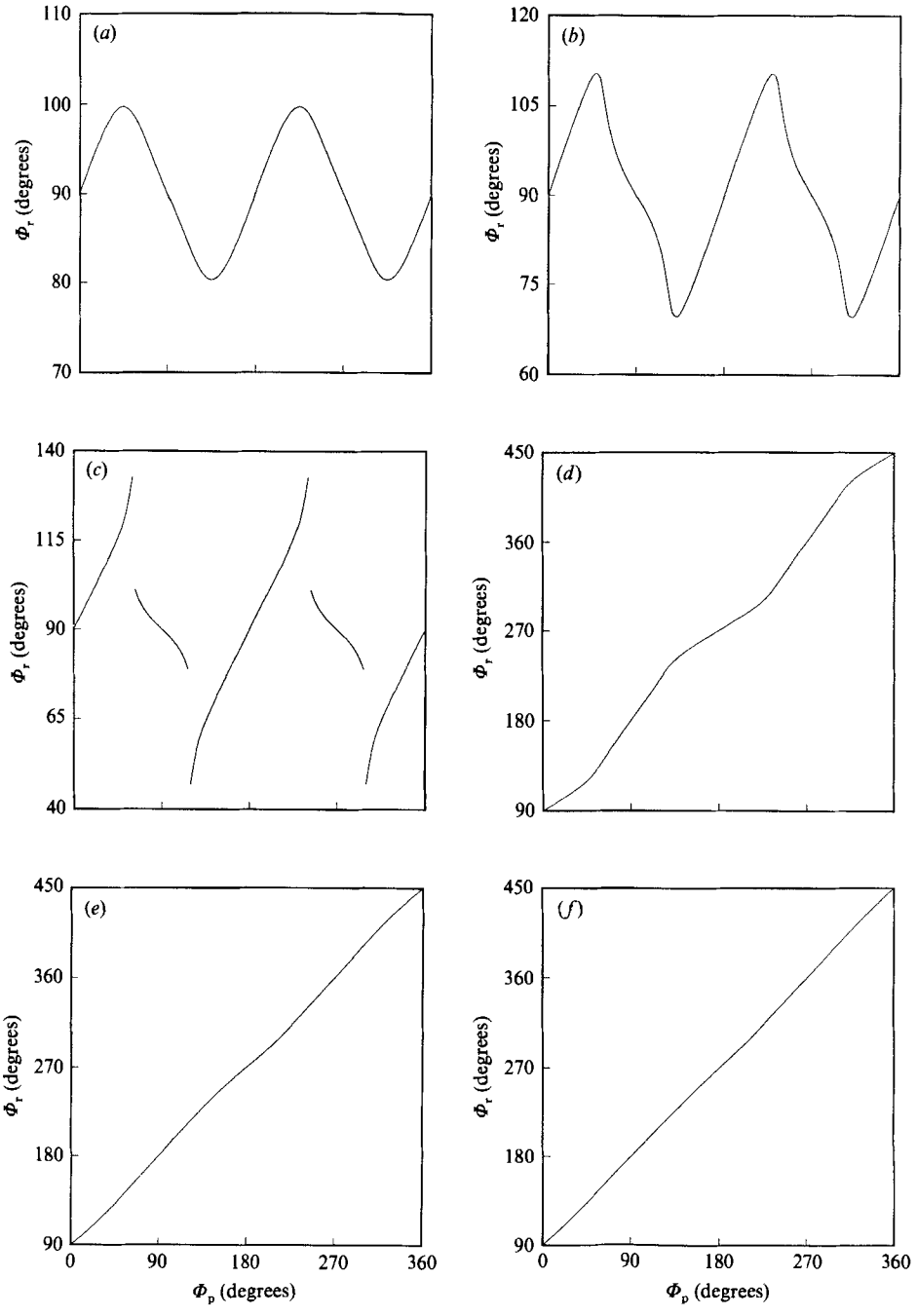

FIGURE 10. Φ_r–Φ_p plots for various h_3 for $h_1 = 0.25$, $h_2 = 0.01$, $h_5 = 0.25$, $\gamma_1 = 0.699$, $\gamma_2 = 3.938\,62$, $\gamma_3 = 0.107$, $\gamma_5 = 0.699$, $\Xi = 4.424\,82$. Plate materials are as in figure 3. The maximum conductivities of the top and bottom plates are in the direction of the x-axis. $\Phi_p = 0°$ corresponds to the maximum conductivity of the middle plate being in the direction of the x-axis. (*a*) $h_3 = 2.5 \times 10^{-4}$, (*b*) $5.468\,75 \times 10^{-4}$, (*c*) $6.953\,125 \times 10^{-4}$, (*d*) 8.4375×10^{-4}, (*e*) 2.625×10^{-3}, (*f*) 5×10^{-3}.

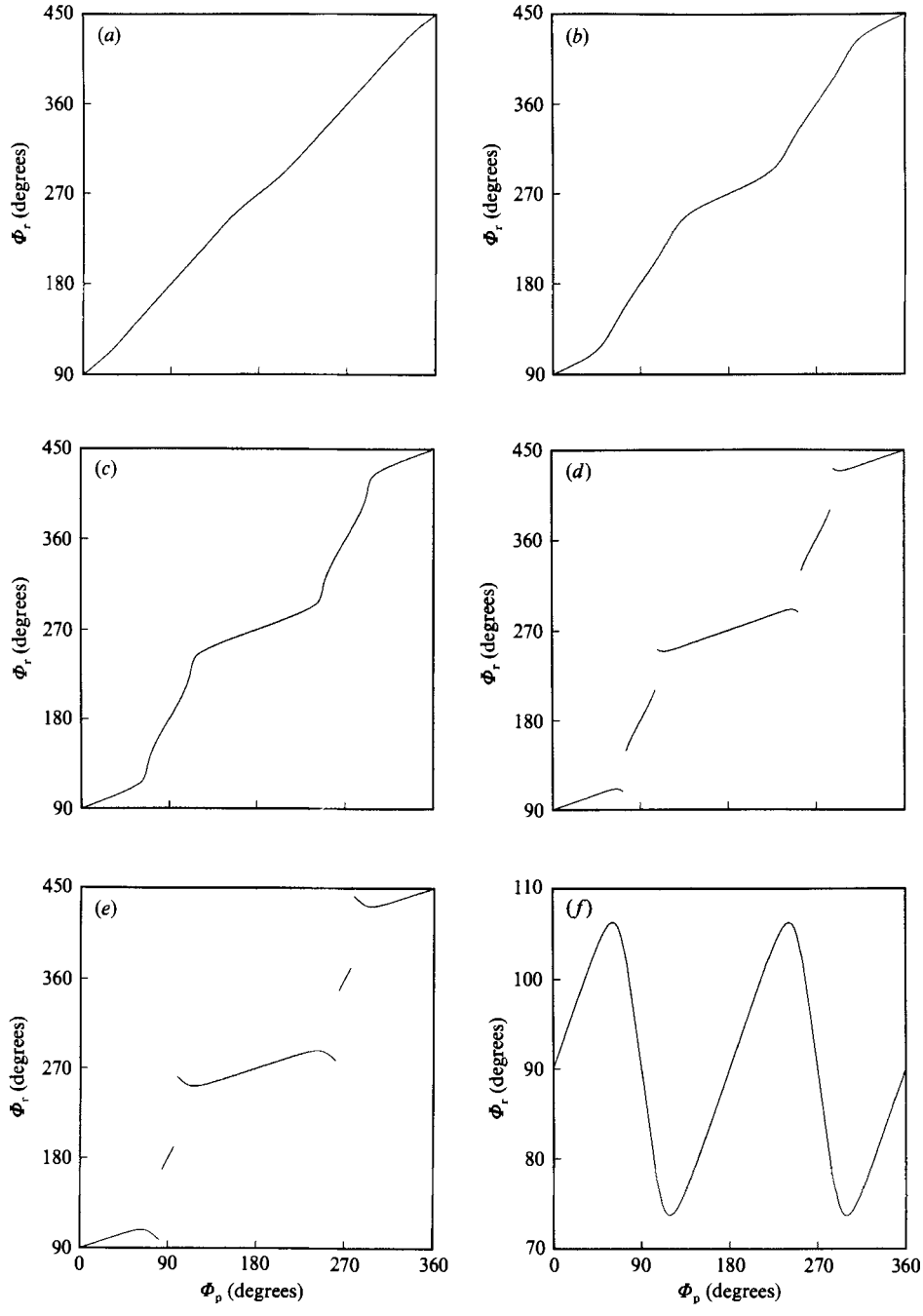

FIGURE 11. Φ_r–Φ_p plots for various h_3 for $h_1 = 0.2$, $h_2 = 0.5$, $h_5 = 0.01$, $\gamma_1 = 0.699$, $\gamma_2 = 3.938\,62$, $\gamma_3 = 0.699$, $\gamma_5 = 0.107$, $\Xi = 4.424\,82$. The top and middle plates are graphite fibre epoxy and the bottom plate is pyrolytic graphite. The maximum conductivities of the top and bottom plates are in the direction of the x-axis. $\Phi_p = 0°$ corresponds to the situation in which maximum conductivity of the middle plate is in the direction of the x-axis. (*a*) $h_3 = 2.5 \times 10^{-3}$, (*b*) 5.625×10^{-4}, (*c*) 4.0625×10^{-4}, (*d*) $3.671\,875 \times 10^{-4}$, (*e*) $3.476\,562\,5 \times 10^{-4}$, (*f*) $3.281\,25 \times 10^{-4}$.

7. Discussion

As shown in the previous section, the middle-plate thickness ratio h_3 is an important parameter in determining how the planform orientation changes with the orientation of the middle plate. For all sets of parameters considered, two limiting cases are obtained, for h_3 very large and very small. As h_3 varies, a smooth transition between the two limiting cases occurs for all cases presented in §6.

For very small h_3, there are several limiting Φ_r–Φ_p topologies. In one, when the maximum conductivities of the top and bottom plates are aligned, Φ_r undergoes a small-amplitude, almost sinusoidal variation about 90° as Φ_p varies from 0° to 360°. When the middle plate is very thin, its thermal anisotropy affects the planform orientation very little. Therefore, Φ_r is determined by the orientations of the top and bottom plates. When the top and bottom plates are oriented in the same direction, with their maximum conductivities in the x-direction, the planform is oriented so that the roll axes are aligned in the y-direction (near $\Phi_r = 90°$). The physical explanation is as follows. When the rolls are oriented with their axes perpendicular to the direction of maximum conductivity in the plates, conduction in the plates makes its maximum possible contribution to the *horizontal* transport of heat in the fluid/solid assembly, and hence convection can be maintained at a lower Ra for this planform orientation than for any other. Therefore, the planform is oriented in the direction which maximizes the horizontal conduction in the fluid/solid assembly. In this particular physical configuration, Φ_r varies about 90° with small amplitude.

However, when the top and bottom plates are aligned so that the directions of their maximum conductivities differ by 90° (figure 8), the limiting case for very small h_3 is an approximately piecewise constant variation of Φ_r with Φ_p, having four branches. For this configuration, the top and bottom plates are identical, except for their orientation. Although the middle plate is very thin, its orientation provides sufficient anisotropy to align the planform in the direction for which the rolls can be maintained at the smallest possible ΔT. In the range $-45° \leqslant \Phi_p \leqslant 45°$, the rolls are aligned with their axes almost exactly in the y-direction. In this situation, the horizontal heat transport is maximized when Φ_r is near 90°. On the other hand, in the range $45° \leqslant \Phi_p \leqslant 135°$, Φ_r varies slightly about 180° (= 0°) since the horizontal heat transport is maximized for rolls aligned in this direction.

In all of the calculations presented in §6, the roll angle is slaved to the plate angle for sufficiently large h_3. When the middle plate rotates once, Φ_r also rotates once. For all cases discussed in §6, the middle plate is oriented so that $\Phi_p = 0°$ corresponds to the largest component of its thermal conductivity being oriented in the x-direction. Therefore, for very large h_3, the planform is oriented in the y-direction for $\Phi_p = 0°$, and as the orientation of the middle plate changes, Φ_r varies almost linearly, with a 90° shift.

The predictions of the present work concern the effect of thermally anisotropic boundaries on convective planform orientation in horizontally unbounded fluid layers. In any real experiment, the planform orientation will also be influenced by the sidewalls, horizontal variations in the boundary conditions, and a number of other experimental details. In any case, the planform and orientation actually realized will correspond to the lowest value of Ra at which convection can be sustained.

To provide a feel for the experimental realizability of some of our more interesting results, we show in figure 12 the relative difference in Ra between the two local minima responsible for the discontinuous Φ_r–Φ_p plot shown in figure 6(*c*). Here, the top and bottom plates are pyrolytic graphite, the middle plate is of graphite fibre

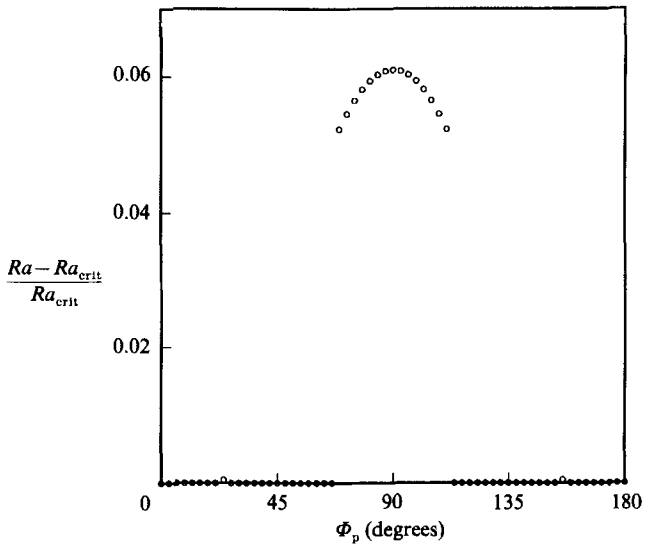

FIGURE 12. Relative difference between Rayleigh numbers at the two local minima on the Ra–a_4 neutral surface shown in figure 6(*c*), for the same materials and thickness ratios. Note that, except for a range of Φ_p centred about 90° with an approximate width of 42°, and two very narrow ranges near $\Phi_p = 24°$ and 156°, the neutral surface is unimodal.

epoxy, and $Ra_{crit} = 4.304 \times 10^4$ is the global minimum on the Ra–a_4 neutral surface. The difference in Rayleigh numbers is a bit more than 6%. This can be contrasted to the degree to which sidewall effects have been eliminated in measurements of the critical Rayleigh number in the standard Rayleigh–Bénard problem ($Ra_{crit} \approx 1707.762\ldots$). In a cell having aspect ratios of 8.0 and 21.3 (width divided by height and length divided by height, respectively) and in one having aspect ratios of 12 and 32, Farhadieh & Tankin (1974) determined $Ra_{crit} = 1700 \pm 20$. This corresponds to a maximum deviation (or uncertainty) of about 1% from the ideal result for a horizontally infinite layer. Thus, for careful experiments in rectangular cells of moderate aspect ratio, a difference in the local minimum values of Ra on the order of 6% between two planform orientations is considerably larger than differences attributable to sidewall effects or other imperfections.

From a physical standpoint, we note that the sidewall effects influence planform orientation (and selection) only through the periphery of the planform, whereas thermal anisotropy of the boundaries acts on the entire planform. Thus, one would expect that for a layered assembly having large but finite aspect ratios, the planform orientation in the interior would be determined by thermal anisotropy of the bounding surfaces, and by sidewall effects near the periphery. One might suppose that if the planform orientation determined by thermal anisotropy in the interior was inconsistent with the geometry of the container, for example, then the interior and peripheral 'domains' of orientation might be mediated by a transitional region of dislocations, as occurs in Rayleigh–Bénard convection when two planform selection/orientation mechanisms compete in the same layer.

A final issue regarding the experimental realizability of our results concerns the question of whether subcritical instability can occur in multilayered anisotropic configurations of the type considered herein. In this regard, we note that for isotropic multilayered configurations, Lienhard (1987) has compared the results of his linear

stability analysis to previous experimental work involving two and three fluid layers separated by conducting plates (Hollands & Wright 1983; Ulrich 1984). He finds that the deviations in Ra_{crit} do not exceed 6%, which is considerably less than the experimental uncertainty in this work. (In the work of Hollands & Wright 1983 and Ulrich 1984, the onset of convection was determined from Nusselt number versus Rayleigh number data, and is considerably less accurate than the interferometric determination of Farhadieh & Tankin 1974.) This provides good reason to believe that subcritical instability (*a*) does not occur in isotropic multilayered systems, and (*b*) will not confound the predictions of our linear stability analysis in the anisotropic case.

The authors thank Professors C. F. Chen and J. C. Heinrich for their careful reading of the MS report of the second author, on which this work is based. The authors gratefully acknowledge support provided by NSF Grant MSM-8451157.

Appendix A

In this Appendix, we define the coefficients

$$\Lambda_{z1} = \frac{\lambda_{+,1}+\alpha_1\lambda_{-,1}+\mathrm{i}(1+\alpha_1)(\epsilon_{xz,1}a_{x1}+\epsilon_{yz,1}a_{y1})}{(1+\alpha_1)h_1\gamma_1/(h_2\gamma_2)},$$

$$\Lambda_{z2}(\alpha_3) = \frac{\lambda_{+,3}e_+ + \alpha_3\lambda_{-,3}e_- + \mathrm{i}(e_+ + \alpha_3 e_-)(\epsilon_{xz,3}a_{x3}+\epsilon_{yz,3}a_{y3})}{(e_+ + \alpha_3 e_-)h_3\gamma_3/(h_2\gamma_2)},$$

$$\Lambda_{z3}(\alpha_3) = \frac{\lambda_{+,3}+\alpha_3\lambda_{-,3}+\mathrm{i}(1+\alpha_3)(\epsilon_{xz,3}a_{x3}+\epsilon_{yz,3}a_{y3})}{(1+\alpha_3)h_3\gamma_3},$$

$$\Lambda_{z4} = \frac{\lambda_{+,5}e'_+ + \alpha_5\lambda_{-,5}e'_- + \mathrm{i}(e_+ + \alpha_5 e_-)(\epsilon_{xz,5}a_{x5}+\epsilon_{yz,5}a_{y5})}{(e'_+ + \alpha_5 e'_-)h_5\gamma_5}.$$

Here we have defined $e_+ = \exp(\lambda_{+,3})$, $e_- = \exp(\lambda_{-,3})$, $e'_+ = \exp(\lambda_{+,5})$, and $e'_- = \exp(\lambda_{-,5})$.

Appendix B

In this Appendix, we define the matrix elements

$$X_{j1}(m,n) = c_{pj}\int_0^1 (\mathrm{D}_j^2 - h_j^2 a_4^2)^2 W_n W_m \,\mathrm{d}z'_j,$$

$$X_{j2}(m,n) = \delta_j h_j^2 a_4^2\left[a_{pnj}\int_0^1 W_m \cosh(h_j a_4 z'_j)\,\mathrm{d}z'_j + e_{pj}\int_0^1 W_m \sinh(h_j a_4 z'_j)\,\mathrm{d}z'_j + c_{pj}\int_0^1 W_m \phi_{nj}\,\mathrm{d}z'_j\right],$$

$$Y_{j1}(m,n) = d_{pj}\int_0^1 W_m(\mathrm{D}_j^2 - h_j^2 a_4^2)^2 W_n \,\mathrm{d}z'_j,$$

$$Y_{j2}(m,n) = \delta_j h_j^2 a_4^2\left[b_{pnj}\int_0^1 W_m \cosh(h_j a_4 z'_j)\,\mathrm{d}z'_j + f_{pnj}\int_0^1 W_m \sinh(h_j a_4 z'_j)\,\mathrm{d}z'_j + d_{pj}\int_0^1 W_m \phi_{nj}\,\mathrm{d}z'_j\right]$$

for $j = 2, 4$ where

$$e_{pn2} = G_2[\mathrm{D}_2\phi_{n2}(0)\,\Lambda_{z1}\cosh a_2 - a_2\,\mathrm{D}_2\phi_{n2}(0)\sinh a_2]$$
$$+ X_2[\Lambda_{z1}\phi_{n2}(1) - \phi_{n2}(0)\,\Lambda_{z1}\cosh a_2 - \mathrm{D}_2\Phi_{n2}(1) + a_2\phi_{n2}(0)\sinh a_2],$$

$$f_{pn2} = V_2[\mathrm{D}_2\phi_{n2}(0)\,\Lambda_{z1}\cosh a_2 - a_2\,\mathrm{D}_2\phi_{n2}(0)\sinh a_2]$$
$$+ Y_2[\Lambda_{z1}\phi_{n2}(1) - \phi_{n2}(0)\,\Lambda_{z1}\cosh a_2 - \mathrm{D}_2\phi_{n2}(1) + a_2\phi_{n2}(0)\sinh a_2],$$

$$c_{p2} = X_2[a_2\cosh a_2 - \Lambda_{z1}\sinh a_2] + G_2[a_2^2\sinh a_2 - \Lambda_{z1}a_2\cosh a_2],$$

$$d_{p2} = Y_2[a_2\cosh a_2 - \Lambda_{z1}\sinh a_2] + V_2[a_2^2\sinh a_2 - \Lambda_{z1}a_2\cosh a_2],$$

$$a_{pn2} = \frac{c_{p2}[\Lambda_{z1}\phi_{n2}(1) - \mathrm{D}_2\phi_{n2}(1)] + e_{pn2}[\Lambda_{z1}\sinh a_2 - a_2\cosh a_2]}{a_2\sinh a_2 - \Lambda_{z1}\cosh a_2},$$

$$b_{pn2} = \frac{d_{p2}[\Lambda_{z1}\phi_{n2}(1) - \mathrm{D}_2\phi_{n2}(1)] + f_{pn2}[\Lambda_{z1}\sinh a_2 - a_2\cosh a_2]}{a_2\sinh a_2 - \Lambda_{z1}\cosh a_2},$$

$$a_{pn4} = X_3[\phi_{n4}(1) + a_4^{-1}\Lambda_{z4}\phi_{n4}(0)\sinh a_4 - a_4^{-1}\mathrm{D}_4\phi_{n4}(0)\sinh a_4]$$
$$+ G_3[-\mathrm{D}_4\phi_{n4}(1) - \Lambda_{z4}\phi_{n4}(0)\cosh a_4 + \mathrm{D}_4\phi_{n4}(0)\cosh a_4],$$

$$b_{pn4} = Y_3[\phi_{n4}(1) + a_4^{-1}\Lambda_{z4}\phi_{n4}(0)\sinh a_4 - a_4^{-1}\mathrm{D}_4\phi_{n4}(0)\sinh a_4]$$
$$+ V_3[-\mathrm{D}_4\phi_{n4}(1) - \Lambda_{z4}\phi_{n4}(0)\cosh a_4 + \mathrm{D}_4\phi_{n4}(0)\cosh a_4],$$

$$c_{p4} = X_3(-\cosh a_4 - a_4^{-1}\sinh a_4\,\Lambda_{z4}) + G_3(a_4\sinh a_4 + \Lambda_{z4}\cosh a_4),$$

$$d_{p4} = Y_3(-\cosh a_4 - a_4^{-1}\sinh a_4\,\Lambda_{z4}) + V_3(a_4\sinh a_4 + \Lambda_{z4}\cosh a_4),$$

$$e_{pn4} = \frac{c_{p4}[\Lambda_{z4}\phi_{n4}(0) - \mathrm{D}_4\phi_{n4}(0)] + a_{pn4}\Lambda_{z4}}{a_4},$$

$$f_{pn4} = \frac{d_{p4}[\Lambda_{z4}\phi_{n4}(0) - \mathrm{D}_4\phi_{n4}(0)] + b_{pn4}\Lambda_{z4}}{a_4},$$

and

$$X_2 = [\lambda_{+,3} + \mathrm{i}(\epsilon_{xz,3}\,a_{x3} + \epsilon_{yz,3}\,a_{y3})]\exp(\lambda_{+,3}),$$

$$Y_2 = [\lambda_{-,3} + \mathrm{i}(\epsilon_{xz,3}\,a_{x3} + \epsilon_{yz,3}\,a_{y3})]\exp(\lambda_{-,3}),$$

$$G_2 = \exp(\lambda_{+,3})\frac{h_3\gamma_3}{h_2\gamma_2}, \quad V_2 = \exp(\lambda_{-,3})\frac{h_3\gamma_3}{h_2\gamma_2},$$

$$X_3 = \lambda_{+,3} + \mathrm{i}(\epsilon_{xz,3}\,a_{x3} + \epsilon_{yz,3}\,a_{y3}), \quad Y_3 = \lambda_{-,3} + \mathrm{i}(\epsilon_{xz,3}\,a_{x3} + \epsilon_{yz,3}\,a_{y3})$$

$$G_3 = h_3\gamma_3, \quad V_3 = h_3\gamma_3.$$

REFERENCES

Ahlers, G. & Behringer, R. P. 1978 Evolution of turbulence from the Rayleigh–Bénard instability. *Phys. Rev. Lett.* **40**, 712–716.

Busse, F. H. 1967*a* On the stability of two-dimensional convection in a layer heated from below. *J. Maths Phys.* **46**, 140–150.

Busse, F. H. 1967*b* The stability of finite amplitude cellular convection and its relation to an extremum principle. *J. Fluid Mech.* **30**, 625–649.

Busse, F. H. & Whitehead, J. A. 1971 Instability of convection rolls in a high Prandtl number fluid. *J. Fluid Mech.* **47**, 305–320.

CARSLAW, H. S. & JAEGER, J. C. 1959 *Conduction of Heat in Solids*, 2nd edn. Oxford University Press.

CATTON, I. & LIENHARD, J. H. 1984 Heat transfer across a two-fluid-layer region. *Trans. ASME* C: *J. Heat Transfer* **106**, 605–612.

CHANDRASEKHAR, S. 1954 On the inhibition of convection by a magnetic field. *Phil. Mag.* **45**(7), 1177–1191.

CHEN, M. M. & WHITEHEAD, J. A. 1968 Evolution of two-dimensional periodic Rayleigh convection cells of arbitrary wave-numbers. *J. Fluid Mech.* **31**, 1–15.

FARHADIEH, R. & TANKIN, R. S. 1974 Interferometric study of two-dimensional Bénard convection cells. *J. Fluid Mech.* **66**, 739–752.

GERSHUNI, G. Z. & ZHUKOVITSKII, E. M. 1976 *Convective Stability of Incompressible Fluids*. Jerusalem: Keter (also available from US National Technical Information Service, Springfield, VA as TT 75-50017).

HIEBER, C. A. 1987 Multilayer Rayleigh–Bénard instability via shooting. *Trans. ASME* C: *J. Heat Transfer* **109**, 538–540.

HOLLANDS, K. G. T. & WRIGHT, J. L. 1983 Heat loss coefficients and effective products for flat-plate solar collectors with diathermaneous covers. *Solar Energy* **30**, 211–216.

JENKINS, M. A. & TRAUB, J. F. 1972 Zeros of a complex polynomial. *Communs Assn Computing Machinery* **15**, 97–99.

LARSON, D. J. 1987 Orbital processing of aligned magnetic composites: flight results from Shuttle mission 51-G. *American Chemical Society, 194th National Meeting, New Orleans, LA, Aug. 30–Sept. 1, 1987.*

LIENHARD, J. H. 1987 An improved approach to conductive boundary conditions for the Rayleigh–Bénard instability. *Trans. ASME* C: *J. Heat Transfer* **109**, 378–387.

PACAGNELLA, L. E. & PIEROBON, G. L. 1976 FFT calculation of a determinantal polynomial. *IEEE Trans. Auto. Control* **21**, 401–402.

PROCTOR, M. R. E. & JONES, C. A. 1988 The interaction of two spatially resonant patterns in thermal convection. Part 1. Exact 1:2 resonance. *J. Fluid Mech.* **188**, 301–335.

ULRICH, T. R. 1984 Heat transfer across a multi-layered air enclosure. MS thesis, University of California, Irvine.